Journal of Computational Neuroscience 14, 161–184, 2003
© 2003 Kluwer Academic Publishers. Manufactured in The Netherlands.

Propagating Waves in Visual Cortex: A Large-Scale Model of Turtle Visual Cortex

ZORAN NENADIC
Division of Engineering and Applied Science, California Institute of Technology, Mail Stop 104-44, Pasadena, CA 91125
zoran@robotics.caltech.edu

BIJOY K. GHOSH
Department of Systems Science and Mathematics, Washington University, Campus Box 1040, One Brookings Drive, St. Louis, MO 63130
ghosh@netra.wustl.edu

PHILIP ULINSKI
Department of Anatomy and Organismal Biology, The University of Chicago, 1025 East 57th Street, Chicago, IL 60637
pulinski@midway.uchicago.edu

Received May 31, 2002; Revised August 14, 2002; Accepted August 29, 2002

Action Editor: Roger Traub

Abstract. This article describes a large-scale model of turtle visual cortex that simulates the propagating waves of activity seen in real turtle cortex. The cortex model contains 744 multicompartment models of pyramidal cells, stellate cells, and horizontal cells. Input is provided by an array of 201 geniculate neurons modeled as single compartments with spike-generating mechanisms and axons modeled as delay lines. Diffuse retinal flashes or presentation of spots of light to the retina are simulated by activating groups of geniculate neurons. The model is limited in that it does not have a retina to provide realistic input to the geniculate, and the cortex and does not incorporate all of the biophysical details of real cortical neurons. However, the model does reproduce the fundamental features of planar propagating waves. Activation of geniculate neurons produces a wave of activity that originates at the rostrolateral pole of the cortex at the point where a high density of geniculate afferents enter the cortex. Waves propagate across the cortex with velocities of 4 μm/ms to 70 μm/ms and occasionally reflect from the caudolateral border of the cortex.

Keywords: visual cortex, large-scale model, cortical waves, Karhunen-Loéve decomposition

1. Introduction

Appearance of a novel stimulus in the visual world produces a wave of activity that propagates across the visual cortex of freshwater turtles. The first evidence for such waves was obtained using extracellular recording methods to study responses evoked in visual cortex by presenting 0.5° spots of light for 100 to 500 ms to alert, paralyzed turtles (Mazurskaya, 1974). Single units throughout the cortex responded to stimuli presented anywhere in binocular visual space, but there were significant latency differences in the responses

of a unit when stimuli were presented at different loci in visual space. This observation raised the possibility that presentation of a visual stimulus produces a wave of activity in the cortex that reaches different cortical loci at different times.

The existence of cortical waves was demonstrated explicitly by Senseman (1996, 1999), who used voltage-sensitive dyes to record the spatiotemporal pattern of activity evoked by whole-field retinal flashes in the visual cortex of an isolated eye-brain preparation. Retinal flashes produced waves of depolarization that consistently originated near the rostrolateral margin of the visual cortex and propagated throughout the cortex. The spread of activity was inhomogeneous, and the propagation velocity was 14 μm/ms rostrally and 40 μm/ms caudally along the rostrocaudal axis of the cortex. Waves were sometimes reflected at the boundaries of the visual cortex, producing secondary waves that propagated into the cortex in the opposite direction. The voltage-sensitive dye signal could be recorded while the membrane potential of individual cortical neurons was recorded with an intracellular microelectrode (Senseman, 1996). The voltage-sensitive dye signal follows closely the membrane potential of individual pyramidal cells. Consistent with the early study by Mazurskaya, Senseman and Robbins (1999) reported that presentation of spots of light at different loci in visual space resulted in waves that differed quantitatively but always originated in the rostral pole of the cortex.

Nenadic et al. (2000) used a simple, biophysically realistic model of turtle cortex to analyze the basic features of the propagating waves. The model represented a 2×12 mm rectangular region of visual cortex. It consisted of 20 pyramidal cells, 4 smooth stellate cells, and 5 geniculate afferents distributed homogeneously in a 4×5 matrix. Each neuron was represented by a compartmental model with realistic synaptic and ionic conductances. Activation of the geniculate afferents produced a propagating wave of activity that was reflected at the cortical boundaries. However, this model did not capture other important features of the waves seen in real cortices, such as the origin of the wave toward the rostral pole of the cortex. Nenadic et al. (2002) used a larger model to show that the propagating waves contain information about the position and speed of moving stimuli. This model is based on the basic distribution of neurons and geniculate afferents within the cortex but does not include some biophysical properties such as spike-rate adaptation. This article provides a full description of this large-scale model and includes spike-rate adaptation in the pyramidal cell models. The model is then used to investigate the origin and fundamental properties of the propagating waves.

2. Organization of Turtle Visual Cortex

A brief account of turtle visual cortex is given here for the convenience of the reader. Ulinski (1990) provides a general discussion of the cerebral cortex of reptiles, including turtles, and Ulinski (1999) gives a detailed discussion of the visual pathways in turtles. The visual cortex of turtles is situated on the dorsolateral surface of the cerebral hemispheres (Fig. 1). It is a three-layered cortex that corresponds to a cytoarchitectonic area designated the dorsal area, D (Colombe and Ulinski, 1999). The intermediate layer 2 contains predominantly the densely packed somata of pyramidal cells. The outer layer 1 and the inner layer 3 contain principally inhibitory interneurons. There are significant differences in the morphology of pyramidal cells

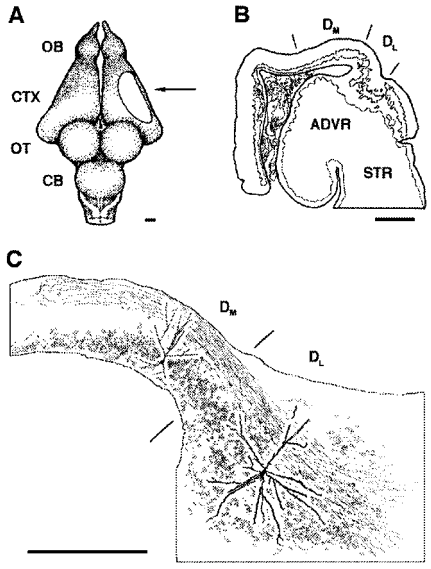

Figure 1. Overview of turtle visual cortex. **A:** Dorsal view of a turtle brain. The oval-shaped area represents the visual cortex, which corresponds to the dorsal area, D. OB, olfactory bulb; CTX, cortex; OT, optic tectum; CB, cerebellum. **B:** Coronal section through the cerebral cortex at the level indicated in A. ADVR, anterior dorsal ventricular ridge; STR, striatum; D_{M}, medial part of D; D_{L}, lateral part of D. **C:** Detailed view of visual cortex showing a medial and lateral pyramidal cell, the positions of cell bodies in layer 2 of D, and the path of geniculate afferents through D. Drawn by Dr. J.B. Colombe.

between the lateral part, D_L, and the medial part, D_M, of area D. Lateral pyramidal cells have their somata packed into large clusters of neurons with opposing somata and have roughly symmetric apical and basal dendritic arbors. Medial pyramidal cells have their somata organized into much smaller clusters and have reduced basal dendritic arbors. Layer 3 is, consequently, thinner in D_M than it is in D_L. Inhibitory interneurons have not been completely characterized, but it is clear that layer 1 contains several populations of inhibitory interneurons and that layer 3 contains horizontal cells with dendrites that run concentric with the ventricular surface.

The dorsal lateral geniculate complex (Rainey and Ulinski, 1986) receives retinotopically organized projections from the entire contralateral retina and from the ventrotemporal rim of the ipsilateral retina (Ulinski and Nautiyal, 1986). Neurons along the rostrocaudal axis of the geniculate project topographically to D but cross over as they enter the lateral margin of the cortex. The rostrocaudal axis of the geniculate is, thus, represented along the caudorostral axis of the cortex. Individual geniculocortical axons course from lateral to medial across D (Heller and Ulinski, 1987). They give rise to relatively few branches but contain many *en passant* varicosities (Mulligan and Ulinski, 1990). There is no indication that neurons situated at different positions along the dorsoventral axis of the geniculate complex project differentially to D. The visual cortex can, consequently, be viewed as a series of isoazimuth lamellae, each receiving information from different elevations at a particular azimuth point in visual space. Neurons in different isoazimuth lamellae receive information from different azimuth lines in visual space via intracortical connections (Cosans and Ulinski, 1990). Neurons in layers 2 and 3 of the cortex project topographically back to the geniculate complex (Ulinski, 1986).

Consistent with the anatomy of the geniculocortical and intracortical projections, single units in visual cortex respond to stimuli presented at all points in visual space (Mazurskaya, 1974). They respond optimally to moving stimuli or to apparent motion stimuli consisting of two spots of light presented at two separate loci in visual space with a temporal delay. Several morphological classes of turtle retinal ganglion cells show directional selectivity and function as local motion detectors (e.g., Jensen and DeVoe, 1983; Granda and Fulbrook, 1989; Ammermuller et al., 1995). It appears that cortical neurons receive convergent input from arrays of local motion detectors and function as global motion detectors (Ulinski, 1999).

3. Construction of Model

3.1. Overview of Model

Waves in turtle visual cortex have been studied by recording from the external surface of the brain using multielectrode arrays (Prechtl, 1994; Prechtl et al., 2000), imaging the external surface of the cortex with voltage-sensitive dyes (Prechtl et al., 1997), or imaging the ependymal surface of the cortex using voltage-sensitive dyes (Senseman, 1996, 1999; Senseman and Robbins, 1999, 2002). Our model is intended to replicate cortical waves imaged on the ependymal surface of the cortex with an in vitro preparation. However, Senseman and Robbins (2002) report that similar waves are recorded from the external surface of the cortex with an in vivo preparation. It is, thus, likely that imaging the ependymal surface of the cortex in vitro gives results that are physiologically relevant. Imaging the ependymal surface is accomplished by cutting along the medial surface of the cortex in an in vitro preparation, unfolding the cortex and pinning it flat in a chamber. The lateral part of the visual cortex is covered by a pallial structure, the dorsal ventricular ridge (DVR), so only D_M and the medial part of D_L are visible in this preparation. Our model consists of an array of 744 neurons that corresponds to the visual cortex as viewed from its ependymal surface. It includes both D_M and all of D_L. Waves produced in the model propagate throughout the entire cortex and can be compared to the data obtained by Senseman and Robbins in vitro.

Emphasis was placed on capturing basic features of the spatial distributions of neurons and geniculate afferents in the cortex and the major features of the physiology of cortical neurons. The relative densities and spatial distributions of four groups of neurons (lateral and medial pyramidal cells, layer 1 stellate cells, and layer 3 horizontal cells) were used in constructing the model. The spatial distributions of stellate cells, pyramidal cells, and horizontal cells were assigned using detailed maps of neurons in each cortical layer that were derived from a complete set of serial coronal sections (Park and Ulinski, unpublished observations). Individual neurons were modeled as equivalent cylinder models based on the morphology of each type of neuron. The firing patterns of neurons in response to intracellular current injections were modeled using

several types of voltage-gated and calcium-dependent conductances, but no effort was made to include details of the kinetics of each conductance or to include all of the conductances that are likely present on these neurons. Geniculate neurons were modeled as single compartmental models with spike-generating mechanisms. The organization of the geniculate axons was based on the detailed anatomy of the geniculocortical projection.

The model, thus, does not include many details of the biophysics and physiology of cortical neurons. However, it does accurately represent the spatial distribution of cortical neurons and geniculate afferents. It also represents the basic circuitry of the cortex, including the excitatory connections of geniculate afferents and intracortical connections and the feedforward and feedback inhibitory circuits.

3.2. *Spatial Distribution of Neurons*

Maps of the spatial distribution of neurons in each of the three layers of the cortex were constructed from alternate coronal sections through the visual cortex of a turtle. The density of neurons was sampled at loci in each of the three layers along the lateromedial axis of each section and used to construct maps of the density of neurons in each layer projected onto the flattened cortical surface. The maps consisted of arrays of 8 × 56 rectangular blocks, each block measuring 28 μm × 190 μm (Fig. 2A). Density measurements were provided for 28 out of 56 columns. The remaining 28 columns represented the alternate sections in which neurons were not counted. Neuronal densities for these sections were linearly interpolated using the densities from adjacent sections.

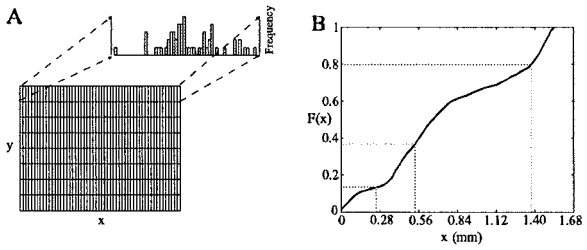

Figure 2. Algorithm for assigning the spatial distribution of cells in the model. **A:** The central part of the figure shows the 8 × 56 grid of rectangles over which neurons were sampled in 28 coronal sections of the cortex of a turtle. Distance along the rostrocaudal axis of the cortex is measured on the x axis. Distance along the lateromedial axis of the cortex is measured on the y axis. The inset shows a histogram of the number of neurons along the top row of the grid. Similar histograms were constructed for the remaining seven rows. **B:** The cumulative distribution function. The grid was used to conduct separate counts of the three layers of the cortex.

Alternate coronal sections through a real cortex were used to construct a map of neurons which represented a smaller total number of neurons but preserved the ratios of neurons in each of the layers. This was done by using data on the numbers of neurons in each row of the real cortical map to construct a cumulative distribution function of the number of neurons in each layer, as a function of distance along the row. A predetermined number of neurons was then sampled from this distribution and used to position neurons in the model. The number of cells in each of the 56 blocks along a given row were used to construct a histogram of the number neurons as a function of distance, x, along the row in the real cortex (Fig. 2A). There were eight such histograms corresponding to the eight rows of the data grid. A cumulative distribution function $F(x)$, was constructed from each of these (Fig. 2B) and used to determine the distribution of neurons in each layer of the model. A total number of n_i neurons were assigned to the ith row in the model data grid and a random vector u_i of n_i numbers was sampled from a uniform distribution between 0 and 1 using the Matlab random number generator. The x-coordinates of n_i points along the ith row of the model data grid were obtained by inverting the cumulative distribution function. If u_{ij} is the value of the jth component of the random vector u_i and if x_{ij} is the x-coordinate of the jth point along the ith row of the model data grid, then we have $x_{ij} = F^{-1}(u_{ij})$. This procedure was repeated for all eight rows of data. The y-coordinates of individual neurons in the ith row were determined by drawing n_i random numbers from a uniform distribution over the 0 to 190 μm interval. This procedure was carried out for each of the three layers resulting in a model that contained 744 neurons. Figure 3 shows the resulting distribution of cells in the model displayed on a single two-dimensional plot. The model has 679 pyramidal cells in layer 2, 45 stellate cells in layer 1, and 20 horizontal cells in layer 3. Of the pyramidal cells, 368 are in D_{L}, and 311 are in D_{M}. These numbers represent scaled-down figures consistent with the relative numbers of layer 1, 2, and 3 cells in the real cortex. An important feature of the map is that the density of pyramidal cells is higher in D_{L} than in D_{M}, while the density of stellate cells is lower in D_{L} than in D_{M}. The ratio of stellate cells to pyramidal

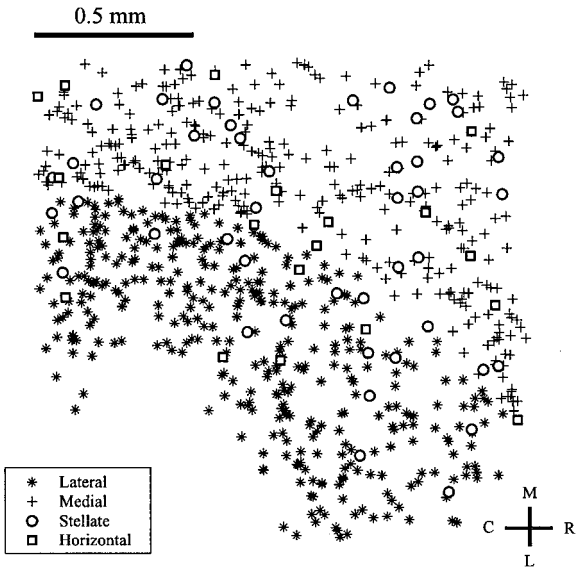

Figure 3. Spatial distribution of neurons in the model. The 744 neurons in the model are shown projected onto a single plane. There are 368 lateral pyramidal cells, 311 medial pyramidal cells, 45 stellate cells, and 20 horizontal cells. Stellate cells (circles) are in layer 1. Pyramidal cells (stars and crosses) are in layer 2. Horizontal cells are in layer 3. The lateral-medial (L-M) and caudal-rostral (C-R) axes of the cortex are indicated.

cells, thus, increases along the mediolateral axis of the cortex.

3.3. *Compartmental Models of Cortical Neurons*

The large-scale model is based on multi-compartmental models of pyramidal (Millonas and Ulinski, 1997), stellate (Khatri and Ulinski, 2000), and horizontal (Nicolaus and Ulinski, 1991) models that have been described earlier. The morphology of each type of neuron in the model was based on a population of neurons impregnated by a variant of the rapid Golgi method (see Colombe and Ulinski, 1999). An individual neuron judged to be the best impregnated of its type was chosen to construct a model. Individual neurons were drawn with a *camera lucida*. The lengths and diameters of dendritic segments were measured using an ocular micrometer. The numbers of spines per 100 μm segment of dendrites on spiny neurons were counted and spine counts corrected for spines hidden behind the dendrites using the algorithm of Feldman and Peters (1979). Spines were folded into the dendritic segment (Stratford et al., 1989) to decrease the number of compartments in the model. Each model

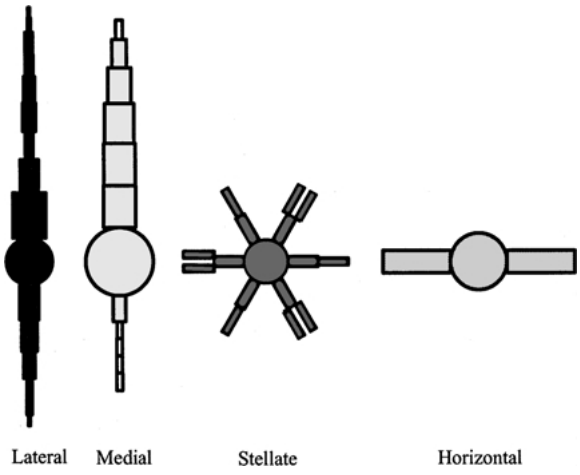

Figure 4. Compartmental models of individual types of neurons. The geometries of the lateral pyramidal, medial pyramidal, stellate, and horizontal cell models are shown. Somata are represented by circular compartments, and dendritic segments are represented by rectangular compartments. The dimensions of individual compartments for each model are given in Appendix A in Tables 1–4.

consisted of a soma compartment and 2 to 15 dendritic compartments, which typically had electrotonic lengths of 0.03. The models captured the basic geometry of the four types of neurons (Fig. 4). Dimensions of each of the compartments in the lateral pyramidal cell model, the medial pyramidal cell model, the stellate cell model, and the horizontal cell model are given in Appendix A in Tables 1–4, respectively.

Each compartment was represented by an ordinary differential equation of the form

$$
\begin{aligned}
-C_i \frac{dV_i(t)}{dt} = \sum_j \frac{V_i(t) - V_j(t)}{R_{ij}} &+ I_{\mathrm{Na}^+}(V,t) \\
&+ I_{\mathrm{K}^+}(V,t) + I_{\mathrm{Ca}^{2+}}(V,t) \\
&+ I_{\mathrm{AHP}}([\mathrm{Ca}^{2+}],t) + I_{\mathrm{Leak}}(V,t) \\
&+ I_{\mathrm{AMPA}}(V,t) + I_{\mathrm{NMDA}}(V,t) \\
&+ I_{\mathrm{GABA_A}}(V,t) + I_{\mathrm{GABA_B}}(V,t), \qquad (1)
\end{aligned}
$$

where $V_i(t)$ is the time-dependent membrane potential of the ith compartment, E_r is the resting membrane potential of the cell, C_i is the total membrane capacitance of the ith compartment, and R_i is the total membrane resistance of the ith compartment. Total resistances and capacitances are calculated from the surface area A_i, of each compartment, the specific membrane

resistance R_m, and specific membrane capacitance C_m, using the relationships $R_i = R_m/A_i$ and $C_i = C_m A_i$. The summation in Eq. (1) is over all of the compartments linked to the ith compartment. R_{ij} is the coupling resistance between the ith and jth compartments given by $R_{ij} = \frac{1}{2}[R_{ai} + R_{aj}]$, where R_{ai} and R_{aj} are the total axial resistances of the ith and jth compartments, respectively. The total axial resistance of the ith compartment is expressed in terms of the specific axial resistance, R_a, by the relationship $R_{ai} = \frac{4lR_a}{\pi d^2}$, where l and d are the length and diameter of the compartment, respectively. A series of current terms represent ionic and synaptic currents and are discussed below.

Passive membrane parameters (R_m, C_m and R_a) for each model neuron were constrained by comparing the responses of model neurons to real pyramidal cells (Mancilla et al., 1998), stellate cells (Khatri and Ulinski, 2000), and horizontal cells (Nicolaus and Ulinski, 1994). Figure 5 shows the response of each type of model neuron to depolarizing and hyperpolarizing current pulses. Membrane parameters in the model cells were systematically varied until the response of the model cell to the lowest-amplitude hyperpolarizing pulse shown in the figure matched the response of the corresponding real cell to within ±0.2 mV for the entire duration of the response. Table 5 in Appendix A gives the membrane parameters estimated for each type of neuron.

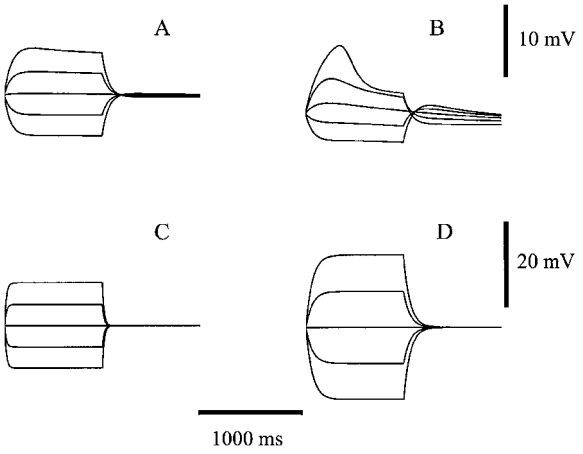

Figure 5. Responses of model neurons to subthreshold current pulses. Simulated responses of the lateral pyramidal cell model (**A**), the medial pyramidal cell model (**B**), the stellate cell model (**C**), and the horizontal cell model (**D**) to subthreshold depolarizing and hyperpolarizing current pulses. Each figure shows the voltage responses of one of the model neurons to two depolarizing and two hyperpolarizing current pulses.

The kinetics of voltage-gated conductances have not been studied using voltage-clamp methods in turtle cortical neurons. However, Connors and Kriegstein (1986) and Colombe and Ulinski (unpublished observations) showed that turtle pyramidal and nonpyramidal neurons have a tetrodoxin-sensitive fast conductance that resembles the classical fast sodium conductance and a cesium-sensitive conductance that resembles the classical delayed rectifier conductance. Thus, fast sodium, $I_{Na^+}(V, t)$, and delayed rectifier potassium, $I_{K^+}(V, t)$, currents were included in all four neuronal models. Both lateral and medial pyramidal cells show a distinct spike-rate adaptation. Spike-rate adaptation typically results from the interaction of a high-voltage calcium conductance and a calcium-dependent potassium conductance (e.g., Madison and Nicoll, 1984). Connors and Kriegstein (1986) found that treatment of turtle pyramidal cells with tetrodotoxin reveals a manganese-sensitive response consistent with the presence of a high-voltage calcium conductance in these cells. This suggests that the mechanism underlying spike-rate adaptation in turtle pyramidal cells resembles that demonstrated in mammals. A high-voltage calcium, $I_{Ca^{2+}}(V, t)$, and a calcium-dependent potassium, $I_{AHP}([Ca^{2+}], t)$, current were, thus, included in the two pyramidal cell models. Pyramidal (Connors and Kriegstein, 1986; Larson-Prior et al., 1991; Mancilla et al., 1998), stellate (Connors and Kriegstein, 1986; Block et al., 2002), and horizontal (Connors and Kriegstein, 1986; Nicolaus and Ulinski, 1994) cells also show evidence of inwardly rectifying conductances that are activated by hyperpolarizing current pulses. These were omitted to minimize the complexity of each model cell and reduce the simulation time required for the full model of the cortex. The steady-state value of the response of each cell type to hyperpolarizing current pulses consequently increases as a linear function of the amplitude of the injected current (Fig. 5). Finally, each of the four model cells had a nonvoltage dependent leak conductance (g_{leak}) that was used to control the resting membrane potentials of the cells. The equations specifying each of the currents are given in Appendix B. Parameter values are given in Table 6 of Appendix B.

Active conductances were modeled by Hodgkin-Huxley-like equations. Since kinetic data were not available, kinetic parameters were modified from those

used in the Traub et al. (1991) model of a CA1 hippocampal pyramidal cell. Parameters were constrained by comparing the responses of each model neuron to real neurons of the same type to depolarizing current pulses. Intracellular calcium dynamics were simulated using an ordinary differential equation that represents the rate of change of intracellular calcium (see Appendix B). No attempt was made to incorporate more complex features of calcium dynamics (e.g., calcium buffering) in the models because appropriate data are not available and, again, we wished to minimize the complexity of the models. The kinetic equations and parameter values are tabulated in Appendix B. Responses of each model cell to depolarizing current pulses that produced subthreshold responses are shown in Fig. 5. Both the lateral (Fig. 5A) and medial (Fig. 5B) pyramidal cells show nonlinear responses due to activation of the high-threshold calcium conductance, while the stellate (Fig. 5C) and horizontal (Fig. 5D) cell models lacked the calcium conductance and did not show nonlinear subthreshold responses. The response of each model cell to a depolarizing current pulse that produced a spike train is shown in Fig. 6. Like real pyramidal cells (Connors and Kriegstein, 1986; Mancilla et al., 1998), the lateral (Fig. 6A) and medial (Fig. 6B) pyramidal cell models show a distinct spike-rate adaptation. Real pyramidal cells often demonstrate firing patterns that resemble intrinsic bursting or chattering firing patterns (Mancilla et al., 1998), but no attempt was made to simulate these firing patterns in this model. Real stellate (Block et al., 2002) and horizontal (Connors and Kriegstein, 1986; Nicolaus and Ulinski, 1994) cells show little or no spike-rate adaptation. Accordingly, the conductances responsible for spike-rate adaptation were not included in the model stellate and horizontal cells, and the stellate (Fig. 6C) and horizontal cell models (Fig. 6D) show no spike-rate adaptation.

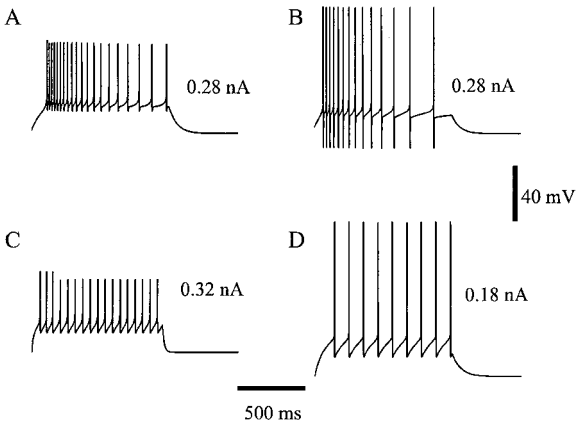

Figure 6. Firing patterns of model neurons. Simulated responses of the lateral pyramidal cell model (**A**), the medial pyramidal cell model (**B**), the stellate cell model (**C**), and the horizontal cell model (**D**) to suprathreshold depolarizing current pulses. Each figure shows the voltage response of one of the model neurons to a depolarizing current pulses with an amplitude large enough to generate a train of action potentials. The amplitude of each current pulse in nA is indicated to the right of each trace.

3.4. Compartmental Model of Geniculate Neurons

Biophysical data are not available for neurons in the dorsal lateral geniculate complex of turtles, so geniculate neurons were modeled as single isopotential compartments with a spike-generating mechanism consisting of a fast sodium and a delayed rectifier potassium conductance. Each geniculate neuron was modeled as a 20.6 μm diameter sphere, with a specific membrane resistance of $R_m = 108$ kΩ cm^2, a specific membrane capacitance of $C_m = 1.4$ μF/cm^2. The kinetic schemes describing the fast sodium and delayed rectifier conductances were the same used in the cortical cells and had maximal conductance densities of $\bar{g}_{Na^+} = 370$ mS/cm^2 and $\bar{g}_{K^+} = 250$ mS/cm^2. Individual neurons were activated by injecting 150 ms, 0.2 nA square current pulses into the compartment. The model contains 201 geniculate neurons. Their axons were modeled as straight lines that extend from lateral to medial across the cortex (Fig. 7A). The most rostral and the most caudal axons in the array extended to the caudal and rostral poles of the cortex, respectively. The 199 other afferents were evenly spaced between these two axons. Propagation along the geniculate afferents was calculated using a conduction velocity of 180 μm/ms at 25°C (Colombe and Ulinski, 1999). Geniculocortical synapses occurred at varicosities that were distributed along the axons. The distribution of varicosities was determined using the distribution of varicosities on real geniculate axons (Mulligan and Ulinski, 1990). One important feature of these axons is that the density of varicosities decreases along the lateromedial axis of the cortex. This can be seen in Fig. 7B, which shows the distribution of varicosities on representative geniculate axons. A second feature is that they enter the cortex through a relatively small region at the rostrolateral pole of the cortex, resulting in a high density of geniculocortical synapses at that point.

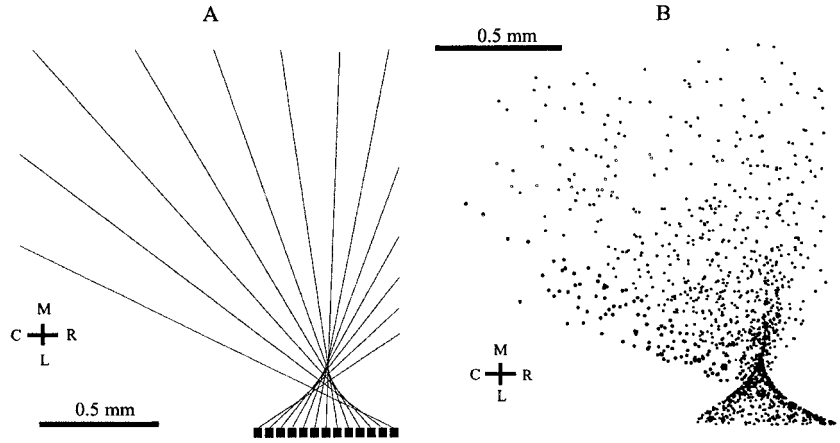

Figure 7. Anatomy of model geniculate neurons. **A:** The organization of the model geniculate neurons and their axons is illustrated, for clarity, with 13 out of the 201 geniculate neurons in the model. The somata of the geniculate neurons are indicated by the linear array of rectangles. Somata are modeled as single compartments with a spike-generating mechanism. Each soma gives rise to an axon that is modeled as a delay line. Consistent with the known anatomy (Mulligan and Ulinski, 1990), axons cross each other as they enter the cortex. **B:** The spatial distribution of varicosities, which are presynaptic sites along all the axons, are shown in this figure. The distribution of varicosities is based on the known distribution of varicosities in geniculocortical axons (Mulligan and Ulinski, 1990). The model contains 1,374 varicosities. Notice the high density of varicosities at the point near the rostral pole of the cortex at which the geniculate axons cross each other.

3.5. Synaptic Connections

3.5.1. Specifying Synapses. Synapses were modeled in two steps. Synaptic currents were constrained using unitary synaptic potentials from real cells, when these were available, or excitatory or inhibitory postsynaptic potentials in other cases. The time courses of synaptic conductances, $g_{\text{syn}}(t)$, were specified using dual exponential functions

$$g_{\text{syn}}(t) = g_{\max} K \left(e^{-\frac{t}{\tau_o}} - e^{-\frac{t}{\tau_c}} \right) \tag{2}$$

when $\tau_o \neq \tau_c$, and where $g_{\max}$ is the density of the synaptic conductance, K is a parameter that scales the function so that its maximal value is $g_{\max}$, τ_o is the open time constant, and τ_c is the close time constant. If, on the other hand, we have $\tau_o = \tau_c = \tau$, then the synaptic conductance is given by

$$g_{\text{syn}}(t) = g_{\max} \frac{t}{\tau} e^{(1-\frac{t}{\tau})}.$$

Maximal conductances and open and close time constants were systematically altered until the voltage traces produced in model cells matched unitary or compound postsynaptic potentials in the real cells. Presynaptic neurons were then connected to all postsynaptic neurons positioned with a sphere of influence that varied according to the kind of connection. Spheres of influence are specified in Table 7 of Appendix B. Synapses were established on the postsynaptic neuron following the connection scheme shown in Fig. 8. The synaptic weight, ω, effected by the presynaptic neuron on postsynaptic cells was specified by either a uniform base synaptic weight, ω_{base}, within the sphere of influence or decreased exponentially following the Gaussian function

$$\omega = \omega_{\text{base}} e^{-\frac{(x_{\text{pre}}-x_{\text{post}})^2+(y_{\text{pre}}-y_{\text{post}})^2}{2\sigma^2}}, \tag{3}$$

where x_{pre}, x_{post}, y_{pre}, and y_{post} are the x- and y-coordinates of the presynaptic and postsynaptic neurons, and σ is a parameter that specifies the rate at which synaptic numbers decrease as a function of distance from the presynaptic neuron. The parameters ω_{base} and σ were constrained by altering them for individual types of synapses until the behavior of propagating waves in the model cortex matched waves recorded by Senseman (1996, 1999) in real cortices. The values of ω_{base} and σ for each type of synapse are shown in Table 8 of Appendix B. No attempt was made to model the more detailed features of synaptic transmission such as synaptic facilitation or depression.

3.5.2. Geniculocortical Connections. Medial pyramidal neurons receive, on average, six times fewer geniculocortical synapses than do stellate neurons

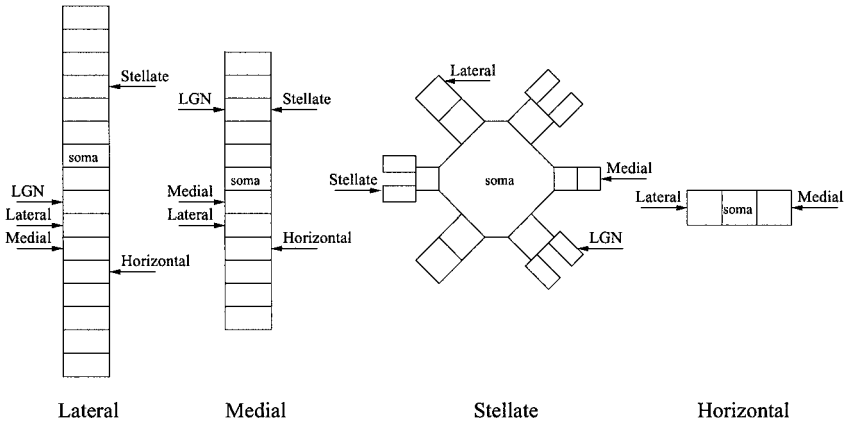

Figure 8. Synaptic connections for model neurons. The compartmental structure of the lateral and medial pyramidal, stellate, and horizontal cell models is shown. Arrows indicate the compartments on which synapses are effected by lateral geniculate neurons (LGN), lateral and medial pyramidal cells, stellate cells, and horizontal cells. Experimental data on which these connections are based are detailed in the text.

(Smith et al., 1980). The spheres of influence for geniculate synapses on pyramidal cells and stellate cells were 60 μm and 25 μm, respectively. Lateral pyramidal cells receive geniculate synapses on their basal dendrites. Medial pyramidal cells receive geniculate synapses on their apical dendrites. Stellate cells rceive geniculate synapses on their dendrites. These distributions correspond to the known distributions of geniculate afferents on real pyramidal cells and layer 1 stellate cells (Colombe and Ulinski, 1999). Geniculocortical synapses on pyramidal cells are glutaminergic and access only the α-amino-3-hydroxy-5-methyl-4-isoxazoleproprionic acid (AMPA) subtype of glutamate receptor (Larson-Prior et al., 1991; Blanton and Kriegstein, 1992). The AMPA-receptor mediated current, $I_{\mathrm{AMPA}}(V, t)$, was constrained using physiological data on minimal excitatory postsynaptic potentials (EPSPs) recorded from pyramidal cells (Mancilla and Ulinski, 1996). The conductance was modeled as a dual exponential function with open and close time constants of $\tau_{\mathrm{o}} = 3.0$ ms and $\tau_{\mathrm{c}} = 0.3$ ms, respectively, and a maximal conductance of $\bar{g}_{\mathrm{AMPA}} = 5$ nS. The reversal potential for geniculocortical synapses has been measured as approximately 0 mV using voltage clamp methods (Blanton and Kriegstein, 1992), and a reversal potential of 0 mV was used in the model. Figures 9A, 10A, and 11A show the responses of the lateral pyramidal cell model, the medial pyramidal cell model, and the stellate cell model, respectively, to a series seven excitatory postsynaptic currents (EPSCs) evoked by activating AMPAergic synapses on the soma compartments of each of the three types of neurons. Each set

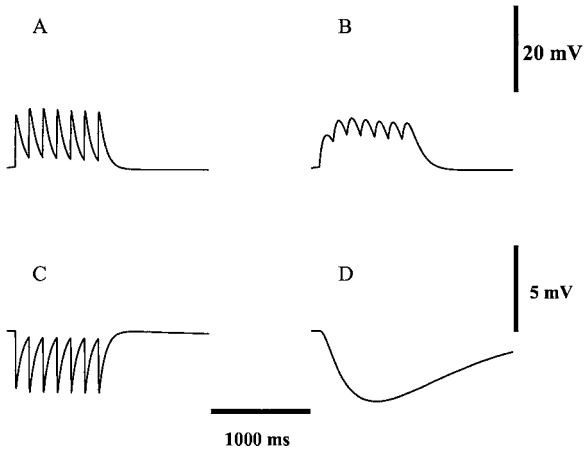

Figure 9. Postsynaptic potentials in the lateral pyramidal cell model. This and the following three figures show the voltage responses evoked in one of the model neurons by activating a particular type of ligand gated receptor on the model. Each trace shows a simulation of an EPSP or IPSP produced by activating a particular type of synapse on the soma compartment. Responses for AMPA, NMDA, and $\mathrm{GABA_A}$-receptor mediated postsynaptic potentials (PSPs) were produced by activating a sequence of seven postsynaptic currents (PSCs). Responses for $\mathrm{GABA_B}$-receptor mediated PSPs were produced by a single PSC. This figure shows EPSPs produced in the lateral pyramidal cell model to AMPA receptor mediated (**A**), NMDA receptor mediated (**B**), $\mathrm{GABA_A}$-receptor mediated (**C**), and $\mathrm{GABA_B}$-receptor mediated (**D**) PSCs.

of EPSPs has relatively rapid rise times, but there are small differences in the shapes of the wave forms that are consistent with the differences in the electrotonic structure of the three types of neurons.

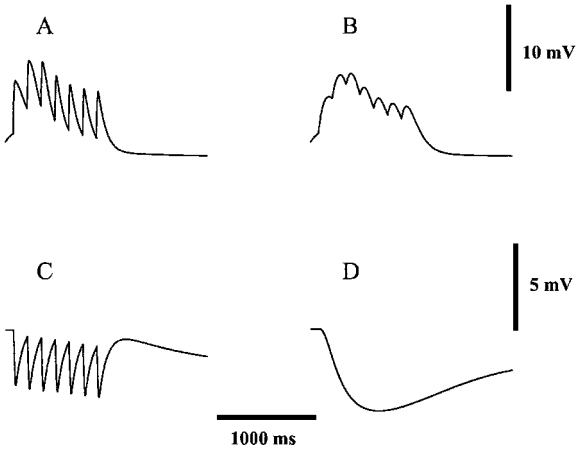

Figure 10. Postsynaptic potentials in the medial pyramidal cell model. This figure shows EPSPs produced in the medial pyramidal cell model to AMPA receptor mediated (**A**), NMDA receptor mediated (**B**), $GABA_A$-receptor mediated (**C**), and $GABA_B$-receptor mediated (**D**) PSCs.

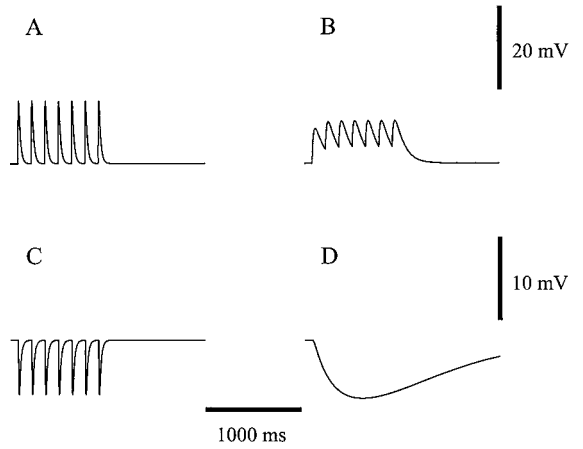

Figure 11. Postsynaptic potentials in the stellate cell model. This figure shows the response of the stellate cell model to AMPA receptor mediated (**A**), NMDA receptor mediated (**B**), $GABA_A$-receptor mediated (**C**), and $GABA_B$-receptor mediated (**D**) PSCs.

3.5.3. Pyramidal Cell Axons. Pyramidal cells have axonal arbors that extend from their somata to the pia in a cone-shaped arbor (Connors and Kriegstein, 1986). Pyramidal cells effect synapses on the basal dendrites of neighboring pyramidal cells and the dendrites of stellate cells. Collaterals of real pyramidal cells also run mediolaterally in layer 3, so model pyramidal cells effect synapses on the dendritic compartments of horizontal cells. Pyramidal cell axons had spheres of influence with radii of 250 μm and synaptic weights that decreased as a Gaussian function of the distance between the presynaptic and postsynaptic cells. Pyramidal cells are glutaminergic and access both the AMPA and N-methyl-D-aspartate (NMDA) subtypes of glutamate receptors on neurons in all three layers of D (Larson-Prior et al., 1991; Blanton and Kriegstein, 1992). Data on miniature AMPA- or NMDA-mediated EPSPs are not available. Postsynaptic currents mediated by pyramidal cell contacts on each type of neuron were modeled as dual exponential functions. The same open and close time constants and maximal conductances used to model geniculocortical AMPAergic conductances were used to model intracortical AMPAergic conductances. Figures 9A, 10A, 11A, and 12A show AMPA-receptor mediated responses in pyramidal, stellate, and horizontal cells. The open and colse time constants and maximal conductances for NMDA-receptor mediated currents, $I_{\mathrm{NMDA}}(V, t)$, were constrained using the late components of intracortical EPSPs recorded from pyramidal cells (Larson-Prior et al., 1991). Values were $\tau_o = 80.0$ ms, $\tau_c = 0.67$ ms, and $\bar{g}_{\mathrm{NMDA}} = 5$ nS. The reversal potential for NMDA receptors is approximately 0 mV (Blanton and Kriegstein, 1992), and a reversal potential of 0 mV was used in the model neurons. The voltage dependence of the NMDA receptors was represented by the factor

$$\frac{1}{1 + 0.33[\mathrm{Mg}^{2+}]\, e^{-0.07(V-60)}} \tag{4}$$

(Jahr and Stevens, 1990), where the extracellular magnesium concentration, $[\mathrm{Mg}^{2+}]$, is 2.0 mM. Figures 9B, 10B, 11B, and 12B show the NMDA-receptor mediated EPSPs produced in the lateral pyramidal, medial pyramidal, stellate, and horizontal cell models, respectively.

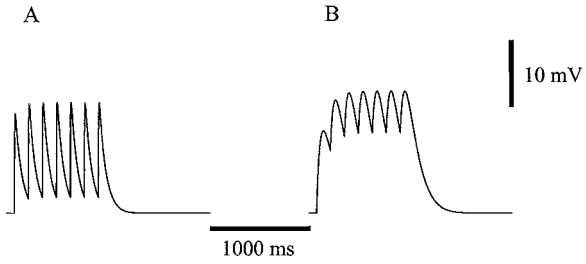

Figure 12. Postsynaptic potentials in the horizontal cell model. This figure shows the response of the horizontal cell model to AMPA receptor mediated (**A**) and NMDA receptor mediated (**B**) PSCs. IPSPs are not shown because the horizontal cells did not inhibit each other in the model.

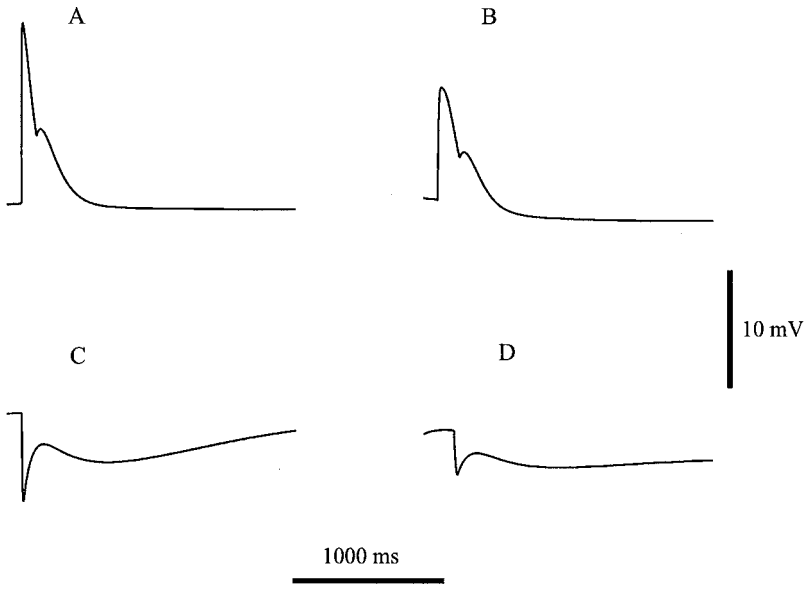

Figure 13. Compound postsynaptic potentials on pyramidal cells. This figure shows the response of the lateral pyramidal cell model (**A, C**) and the medial pyramidal cell model (**B, D**) to simultaneous activation of AMPA and NMDA receptor-mediated EPSCs (**A, B**) and $GABA_A$- and $GABA_B$-receptor-mediated IPSCs (**C, D**).

Intracortical stimulation produces compound EPSPs in pyramidal cells, suggesting that intracortical afferents access both AMPA and NMDA receptors on their postsynaptic targets (Larson-Prior et al., 1991). Figure 13A and 13B show the compound EPSPs produced in the lateral pyramidal and medial pyramidal cell models, respectively, by simultaneous activation of AMPAergic and NMDAergic conductances on their soma compartments. These simulations capture the biphasic EPSPs seen in real cortical neurons following intracortical stimulation (Larson-Prior et al., 1991).

3.5.4. Axons of Inhibitory Interneurons. Stellate cells have their somata located in layer 1 and have spherical regions of influence with radii of 350 μm. Model stellate cells effect synapses on the apical dendrites of pyramidal cells and dendrites of neighboring stellate cells but effect no synapses on the horizontal cells. Their axons have spheres of influence with the above diameter and uniformly distributed synaptic weights. Both pyramidal and stellate cells show fast and slow inhibitory postsynaptic potentials (IPSPs) that are mediated by $GABA_A$ and $GABA_B$ receptors, respectively. Data on presumptive miniature $GABA_A$ receptor-mediated IPSPs in pyramidal (Fowler, 1994) and stellate (Khatri and Ulinski, 2000) neurons were used to constrain the time courses of $GABA_A$ receptor-mediated currents, $I_{GABA_A}(V, t)$, in model neurons that receive inhibitory contacts by stellate cell axons. Values were $\tau_o = 1.7$ ms, $\tau_c = 1.7$ ms, and $\bar{g}_{GABA_A} = 5$ nS. $GABA_A$-receptor mediated conductances have measured reversal potentials near the chloride receptor potential (Blanton and Kriegstein, 1992), and a reversal potential of -70 mV was used in each of the model neurons. Figures 9C, 10C, and 11C show the responses of the lateral pyramidal, medial pyramidal, and stellate cell models to a sequence of seven $GABA_A$-receptor mediated IPSCs. No data on miniature $GABA_B$-receptor mediated currents, $I_{GABA_B}(V, t)$, are available. The time courses of $GABA_B$-receptor mediated conductances were thus constrained using the time courses of slow IPSPs (Khatri and Ulinski, 2000). Values were $\tau_o = 500$ ms, $\tau_c = 500$ ms, and $\bar{g}_{GABA_B} = 5$ nS. $GABA_B$-receptor-mediated currents have measured reversal potentials near the potassium reversal potential (Blanton and Kriegstein, 1992), and a reversal potential of -90 mV was used in each of the model neurons. Figures 9D, 10D, and 11D show the responses of the model lateral pyramidal cell, the model medial pyramidal cell, and the model stellate cell, respectively, to a single $GABA_B$-receptor mediated IPSP generated on the soma compartment. Both pyramidal cells (Ulinski et al., 1991) and stellate cells (Khatri and Ulinski, 2000)

show compound IPSPs following activation of geniculate afferents, suggesting that stellate cells access both $GABA_A$ and $GABA_B$ receptors on pyramidal cells and stellate cells. Figures 13C and 13D show the compound IPSPs produced in the lateral pyramidal and medial pyramidal cell models by simultaneous activation of $GABA_A$- and $GABA_B$-receptor-mediated IPSCs in the two types of cells. Comparable compound IPSPs were produced in stellate cells (not shown).

Horizontal cells have their somata located in layer 3. The morphology of horizontal cell axons is not known. Model horizontal cells have a sphere of influence with a radius of 350 μm and a uniform distribution of synaptic weights. In the model, they effect synapses on the basal dendrites of the pyramidal cell model. Horizontal cells show GABA-like immunoreactivity to anti-GABA antibodies (Nicolaus and Ulinski, 1991; Blanton et al., 1987), but nothing is known about the physiology of their postsynaptic contacts. It was assumed that horizontal cells access both $GABA_A$ and $GABA_B$ receptors on their postsynaptic targets and that the time courses of the two types of conductances are the same as those occurring in the synapses of stellate cells on cortical neurons. The compound IPSPs produced in the lateral and medial pyramidal cell models, thus, were the same as the stellate cell-mediated IPSPs shown in Figures 9–11.

3.6. Simulations

Diffuse retinal flashes were simulated by injecting square current pulses of 150 ms duration simultaneously into all 201 geniculate neurons. Spots of light flashed on the retinal surface were simulated by simultaneously activating groups of 20 geniculate neurons for 150 ms. The model was implemented using Genesis (Bower and Beeman, 1997). Simulation of a 1,500 ms response of the model cortex typically required three hours on a Dell Precision Workstation with 1 Gbyte of RAM and a 1 GHz processor speed. The membrane potentials of examples of individual neurons were examined. The behavior of the entire population of neurons was examined by preparing movies of the responses. To do this, individual membrane potentials were spatially resampled from a nonuniform grid, determined by the locations of the neurons, to a uniform grid of pixels using Matlab. Movies representing the results of simulations were obtained using Matlab imaging tools. These movies are comparable to those obtained using voltage-sensitive dye methods by Senseman (1999), Senseman and Robbins (1999, 2002), and Robbins and Senseman (1998).

4. Results

Figure 14 shows the responses of a sample of eight model pyramidal cells from different regions of the cortex to a simulated diffuse light flash. Figure 15 shows responses from sixteen additional model pyramidal cells arranged along lateral to medial (Fig. 15A) and rostral to caudal (Fig. 15B) transects of the model cortex. A total of 23 of the 24 cells respond to the stimulus with a postsynaptic potential and a train of action potentials; the remaining cell shows only a postsynaptic potential (PSP). Similarly, many of the 679 pyramidal cells in the model and a significant fraction of real layer 2 regular spiking cells (Mancilla et al., 1998) show postsynaptic potentials but no action potentials in response to diffuse retinal flashes. Diffuse light flashes typically produce only a few action potentials in pyramidal cells (Kriegstein, 1987; Senseman, 1996; Mancilla et al., 1998; Mancilla and Ulinski, 2001). The model pyramidal cells generally produced more action potentials in response to simulated light flashes than do real pyramidal cells.

The latencies of the responses vary with the position of the cells in the cortex. Cells situated at the rostrolateral pole of the cortex, near the entry point of the geniculate fibers to the cortex, have the shortest latencies. Cells situated toward the caudolateral pole of the cortex have the longest latencies. This point can be seen clearly in the vertical transect in Fig. 15A. Cell A is situated near the rostrolateral pole of the cortex and has a short latency. Cells B through H are situated at progressively greater distances from the rostrolateral pole of the cortex and have successively longer latencies. Along the horizontal transect in Fig. 15B, cell A has the shortest latency, while the latencies increase slightly toward the rostral edge of the cortex (compare cells B, C, and D) and more significantly toward the caudal edge of the cortex (compare cells E through H). These systematic shifts in response latency in individual cells are consistent with the records obtained by Mazurskaya (1974) in the visual cortex of paralyzed turtles and with the existence of a wave of activity that begins at the rostrolateral pole of the cortex and propagates across the cortex (Senseman, 1996, 1999).

Such a wave can be seen explicitly in movies of the model cortical response that are comparable to the

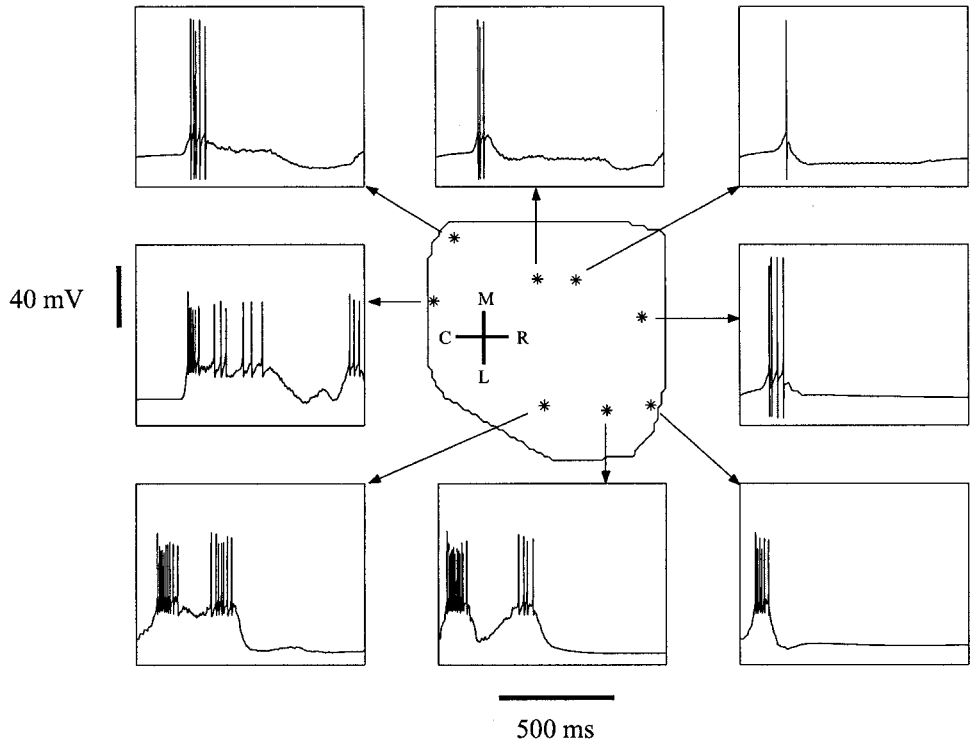

Figure 14. Responses of model pyramidal cells to a simulated light flash. This figure shows the responses of eight model pyramidal cells to a simulated light flash. Each box shows the voltage response of an individual lateral pyramidal cell model or medial pyramidal cell model. Medial pyramidal cell responses are distinguished by strong after-hyperpolarizations. The position of each cell in the cortex is indicated by an asterisk. The outline of the model cortex is shown in the center of the figure. The caudal-rostral (C-R) and lateral-medial (L-M) axes of the cortex are indicated.

movies prepared by Senseman (1999) and Senseman and Robbins (1999, 2002) for turtle cortices. Figure 16 shows individual frames from a representative movie. The color scale indicates the membrane potential at a particular locus in the cortex at a particular time. The response begins at the rostrolateral pole of the cortex at about 10 ms. Figure 17 shows selected frames from movies of waves produced by activating groups of geniculate afferents that correspond to presenting spots of light to nasal, temporal, and central points along the nasal-temporal axis of the retina. The wave begins in the same general region of the cortex at about 15 ms poststimulus in each case. There are small differences in the origin of the wave between the cases. However, it is unlikely that these could be resolved with voltage-sensitive dye methods. The model is, thus, consistent with voltage-sensitive dye data in showing that the cortical wave is invariably initiated at the rostrolateral pole of the cortex. After its initiation, the wave propagates across the cortex for approximately 600 ms, at which time it reaches a peak at the caudomedial pole of the cortex. This occurs at 570 ms in Fig. 16 but is not shown in Fig. 17 (which focuses on the first 200 ms of the response). The wave subsequently begins declining in amplitude and is usually completed between 1,200 ms and 1,500 ms.

The propagation velocity of the wave can be quantified in two different ways. The first is in the form of an isolatency map that represents the half-height latencies of the wave as contours superimposed on the cortex (Senseman and Robbins, 2002). Figure 18A shows an isolatency map for the experimental wave (Senseman, 1999) superimposed on a picture of a real turtle cortex and adjacent anterior dorsal ventricular ridge (ADVR). The boundary between visual cortex (cytoarchitectonic area D) and the dorsomedial cortex (DM) is indicated by the dotted line. Latencies between 150 ms and 280 ms are indicated by the color scale. Figure 18B shows a similar plot for the model cortex. Note that only area D is included in this plot and

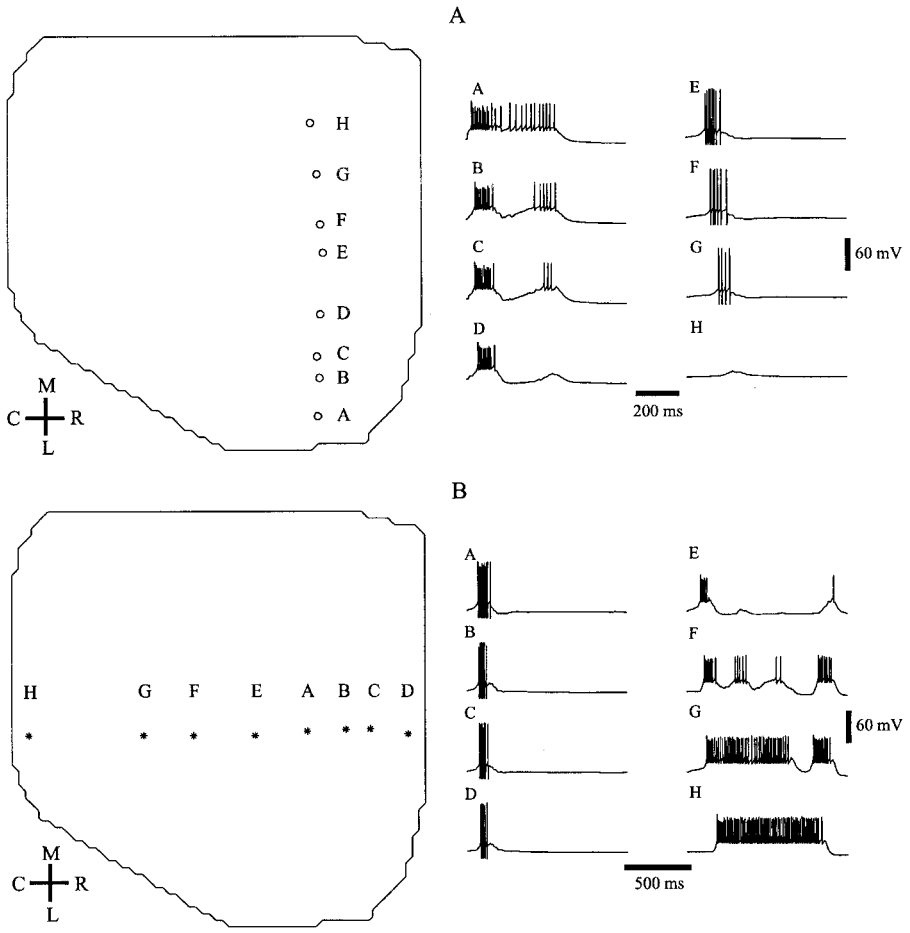

Figure 15. Responses of model pyramidal cells to a simulated light flash. Latency differences between pyramidal cells at different positions in the model. This figure illustrates the differences in firing responses of neurons along a vertical (**A**) and horizontal (**B**) transect through the cortex. Each figure shows an outline of the cortex on the left. The caudal-rostral (C-R) and lateral-medial (L-M) axes of the cortex are indicated. The positions of eight pyramidal cells are indicated by letters. Cells A through D in the top figure (A) are lateral pyramidal cells; cells E through H are medial pyramidal cells. In the bottom figure (B), the cells labeled by A, B, C, and D are medial pyramidal, and the cells labeled by E, F, G, and H are lateral pyramidal cells. The response of each pyramidal cell is shown in a voltage trace to the right of each figure. Medial pyramidal cell responses are distinguished by strong after-hyperpolarizations.

that the spatial scale is different from that of Fig. 18A. The point at which geniculate axons enter the cortex is represented by a notch at the rostrolateral edge of the cortex in both figures. Notice that latencies are lowest at this notch and increase along both the lateromedial and rostrocaudal axes of both cortices. The details of the propagation velocities are easier to see in plots of the half-height latency of the wave as a function of distance along transects across the cortex (Senseman, 1999). Figure 18(C) shows plots of the latency of the wave along a vertical (or lateromedial) transect, a horizontal (or rostrocaudal) transect, and a diagonal transect that runs from the rostrolateral to the caudomedial poles of the model cortex. The propagation velocity at any point in the cortex is the reciprocal of the slope of line in the plot at that particular point. In the vertical transect, the wave propagates toward medial edge of the cortex with a velocity of 65.8 μm/ms and toward the lateral edge of the cortex with a velocity of 4.4 μm/ms. In the horizontal transect, the wave propagates rostrally with a velocity of 4.6 μm/ms and caudally with an initially velocity of 12.8 μm/ms slowing to a final velocity of 3.5 μm/ms. A comparable slowing occurs in turtle cortex, which is represented by the increasing distance between successive isolatency contours in Fig. 18A along a transect from the entrance of

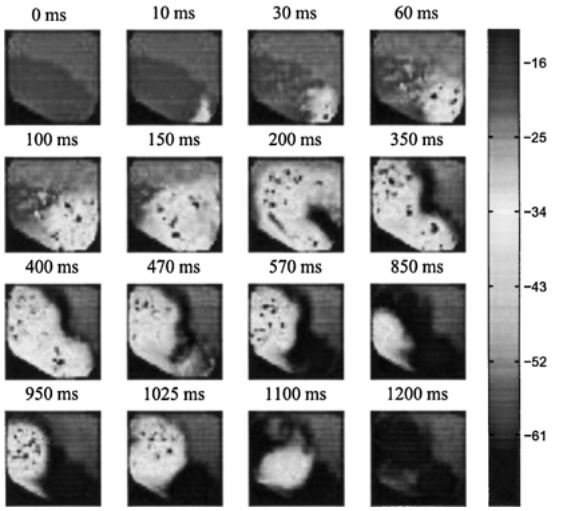

Figure 16. Response of the model cortex to a diffuse light flash. This figure shows a series of snapshots from a movie of the response of the model cortex to a simulated light flash. The first frame (0 ms) shows the model at the time of the simulated flash. Each frame shows a view of the cortex that corresponds to the flattened cortex shown in Fig. 3. The color scale indicates the level of depolarization (warm colors) or hyperpolarization (cold colors). The numbers to the right of the scale show the values of the membrane potential in (mV) coded by a particular color. For a color print of this figure, go to http://www.cbcis.wustl.edu/pubs/turtle/jcns/fig16.pdf.

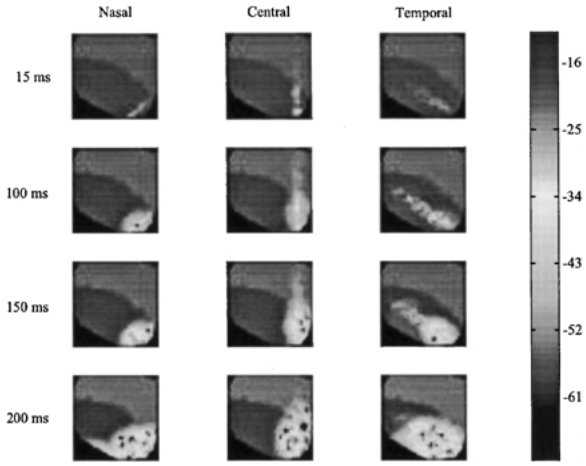

Figure 17. Response of the model cortex to a restricted light flashes. This figure shows a series of snapshots from movies of the responses of the model cortex simulations of spots of light presented to the nasal, central and temporal retina (from left to right). The top line of the frames show the model 15 ms after the simulated flashes. Subsequent frames below show the model at the indicated times after the simulated flashes. Each frame shows a view of the cortex that corresponds to the flattened cortex shown in Fig. 3. The scale to the right indicates the level of depolarization (warm colors) or hyperpolarization (cold colors). The numbers to the right of the scale show the values of the membrane potential in (mV) coded by a particular color. For a color print of this figure, go to http://www.cbcis.wustl.edu/pubs/turtle/jcns/fig17.pdf.

the geniculate fibers to the caudal edge of the cortex. The anisotropy between the propagation velocities of the wave towards the medial and caudal edges of the cortex is represented by the difference in the spacing of isolatency contours along the lateromedial and rostrocaudal transects in Fig. 18B. In the diagonal transect, the wave propagates with a uniform velocity of 8.1 μm/ms.

After the wave reaches the caudolateral pole of the cortex, there is sometimes a secondary depolarization, or reflection, of the wave at the caudal edge of the cortex. This is seen as a second, late cluster of action potentials in the cell shown in Fig. 14 (left, middle trace) and as a prolonged sequence of action potentials in Fig. 15 (trace H of the bottom figure), which continues as bursts of action potentials with progressively longer latencies in Fig. 15B, traces G, F, and E. Notice that the reflected wave dies out as it propagates along the caudorostral axis, as indicated by the decreasing numbers of action potentials in Fig. 15B, traces G, F, and E.

Robbins and Senseman (1998) and Senseman and Robbins (2002) have shown that the spatiotemporal dynamics of the waves can be conveniently represented in a low-dimensional phase space, A, using Karhunen-Loéve decomposition, which is a variant of principal component analysis. The movie, $I(x, y, t)$, of a wave is used to construct a correlation matrix. The eigenfunctions, $\psi_i(x, y)$, of the correlation matrix and the projections of the movie data on the ith respective modes, $\alpha_i(t)$, are then calculated. The eigenfunctions depend on the spatial coordinates of the cortex. Movies can be accurately reconstructed using the first two or three eigenfunctions:

$$I(x, y, t) \approx \sum_{i=1}^{3} \alpha_i(t)\psi_i(x, y). \tag{5}$$

The dynamics of the wave can consequently be represented by a trajectory in a three-dimensional phase space, A, of the vector function, $(\alpha_1(t), \alpha_2(t), \alpha_3(t))$. The same analysis can also be performed on waves generated by simulated diffuse flashes or by localized spots of light on the model cortex (Nenadic et al., 2002). Figure 19A shows the three principal eigenfunctions, or spatial modes, obtained from a single wave resulting from a simulated light flash. Figure 19B shows the time courses of $\alpha_1(t)$, $\alpha_2(t)$, and $\alpha_3(t)$, and Fig. 19C

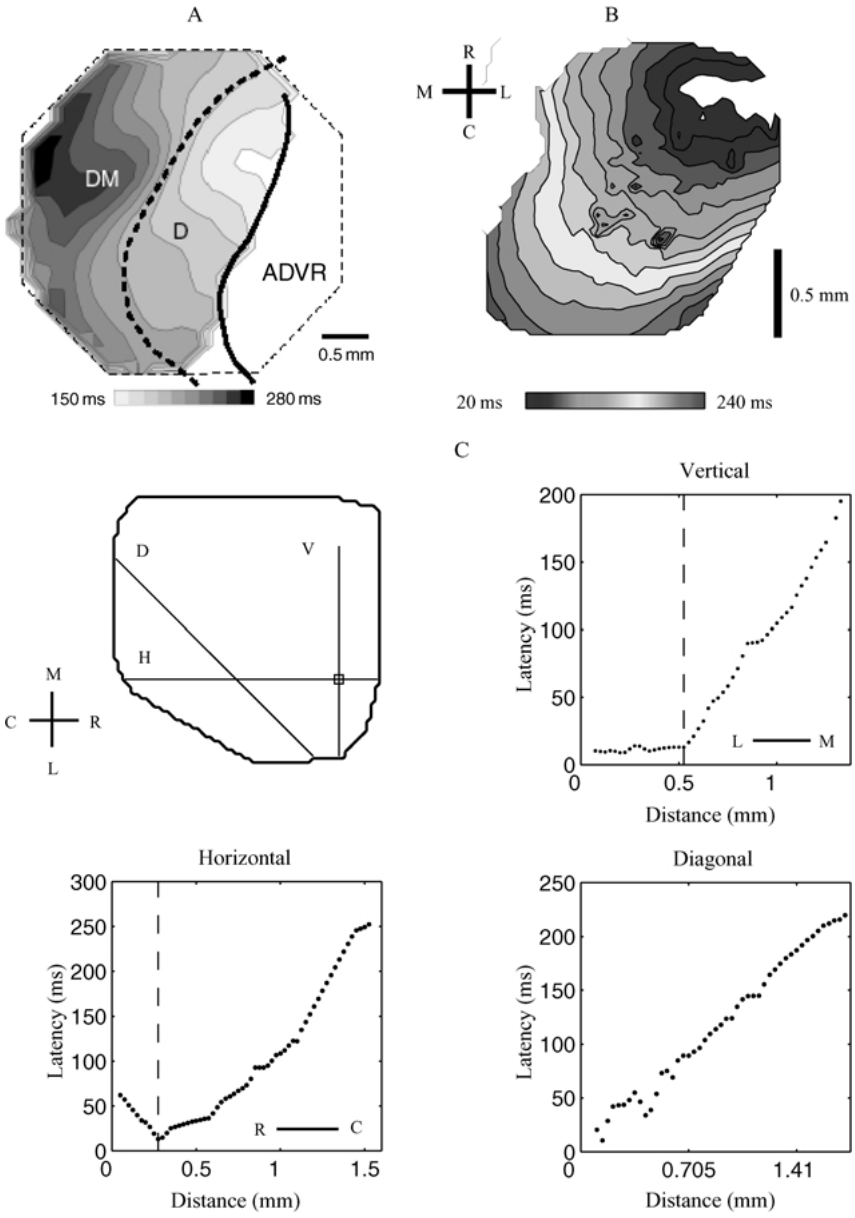

Figure 18. Response latencies following a simulated light flash in real and model cortices. Latency is measured as the time at which the wave reaches its half maximal value. Data are presented in two forms. The top two figures are isolatency maps in which latency is represented by a color scale. **A:** The map shows an isolatency map for the experimental wave (Senseman, 1999) superimposed on a picture of a real turtle cortex. It shows the lateral (D_L), medial (D_M) parts of visual cortex and the border of D_L with the anterior dorsal ventricular ridge (ADVR) at a relatively low magnification (from Senseman, 1999). **B:** The map shows D_L and D_M in the model. **C:** The plots show the latency of the response as a function of distance along vertical, horizontal, and diagonal transects of the model cortex. The three transects are indicated on the outline of the model shown at the upper left. For color of 18(B) of this figure, go to http://www.cbcis.wustl.edu/pubs/turtle/jcns/fig18B.pdf.

shows the three-dimensional trajectory of the vector $\alpha_1(t), \alpha_2(t), \alpha_3(t)$ in the A-space. The state of the model cortex prior to activation corresponds to an initial point in A-space. The point moves away from this initial point in an elliptical, or tear-drop, shaped orbit that reaches a maximal distance from the initial point and then turns and moves back toward the initial point. In general, the spatial modes must be global and should

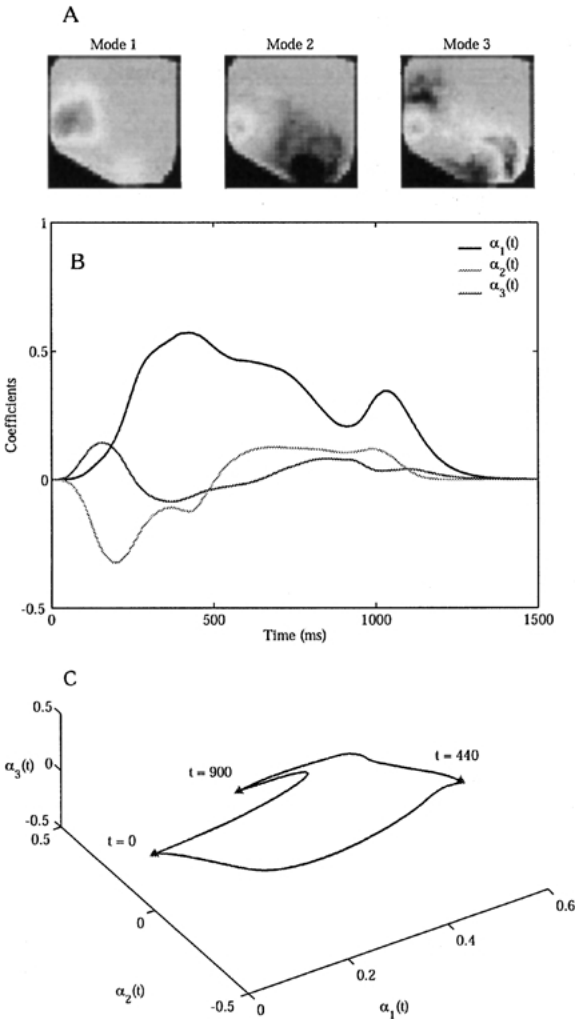

Figure 19. Karhunen-Loéve analysis of the cortical response. **A:** Plots of the first three eigenfunctions in the Karhunen-Loéve decomposition of a cortical response. **B:** Time courses of the weights corresponding to the first three principal eigenfunctions. **C:** Phase plane plot of the weights in (B).

therefore be averaged over multiple simulations resulting from the model cortex. This can be achieved by adding a random noise to the model cortex and is a subject of future investigation.

5. Discussion

This article presents a large-scale model of turtle visual cortex that represents the spatial distribution of cortical neurons and geniculate afferents and the basic circuitry of the cortex. Simulations of the responses of the model to diffuse retinal flashes and spots of light presented at different loci along the horizontal meridian produce propagating waves.

5.1. Features and Limitations of the Model

An earlier model (Nenadic et al., 2000) of turtle visual cortex showed that a propagating wave could result from relatively simple synaptic interactions. However, this model did not capture the more complex dynamics of the cortical waves seen in voltage-sensitive dye experiments. This is not surprising because the model did not have the particular spatial distributions of neurons seen in the real cortex and did not incorporate the geometry of the geniculocortical afferents. The goal in constructing the current model was to include some of the fundamental features of turtle visual cortex in an attempt to more accurately portray the spatiotemporal dynamics of turtle visual cortex. The spatial distribution of neurons in each of the three layers of the cortex is based on an accurate map of neurons in turtle visual cortex. The model includes some of the differences in the anatomy of lateral and medial pyramidal cells and the basic anatomy of two groups of inhibitory interneurons, layer 1 stellate cells and layer 3 horizontal cells. Stellate and horizontal cells appear to be involved in establishing feedforward and feedback inhibitory circuits, respectively, within the cortex. The model also captures the geometry of the geniculocortical afferents, including a detailed representation of the density of varicosities on the geniculate axons as a function of position in the cortex.

However, the model has several important limitations. First, physiological data on ligand gated receptors and voltage gated channels were included wherever possible, but most aspects of the physiology of turtle cortical neurons are incompletely known. The basic pharmacology of synapses has been studied, but many details, such as potential kinetic differences between different types of synapses within the cortex, have not been examined. The basic distinction between regular spiking neurons, which show a distinct spike-rate adaptation, and fast-spiking neurons that show little or no spike-rate adaptation are included in the model. However, there have been no voltage clamp studies of the kinetics of voltage-gated channels in turtle cortex, and it was necessary to modify kinetic data from work on mammalian cortex for the model. The full range of conductances that are likely present on turtle cortical neurons was not included. For example,

several types of cortical neurons probably have hyperpolarization activated conductances that were not included. There is also reason to believe that the dendrites of pyramidal cells have active conductances (Connors and Kriegstein, 1986; Millonas and Ulinski, 1997) that were not included in the model pyramidal cells. Some evaluation of the consequence of choosing particular values of parameters in modeling ligand-gated receptors and voltage-gated channels on the behavior of the model cortex can be obtained by varying these parameters in a series of simulations. A full discussion of these effect is beyond the scope of this article. However, it is clear from preliminary simulations that features of the cortical waves, such as their propagation velocities and durations, do depend on cellular parameters such as the density of inhibitory receptors and the presence of spike-rate adaptation in the model pyramidal cells.

A second limitation of the model is that the input to the cortex is unrealistic. The input is a linear array of geniculate neurons that does not capture the spatial distribution of neurons in the turtle dorsal lateral geniculate complex (see Rainey and Ulinski, 1986). Model geniculate neurons were used to generate a spike train that activated cortical neurons. However, no attempt was made to accurately model spike trains of real geniculate neurons, which have not been well characterized. The visual cortex gives rise to a feedback projection to the geniculate complex (Ulinski, 1986). This projection was not included in the model and seems likely to influence the dynamics of the cortex by prolonging the duration of cortical responses. The firing patterns of retinal ganglion cells are also likely to produce ongoing responses in the cortex because ganglion cells frequently respond to even brief light flashes with trains of action potentials that last a second or more (e.g., Marchiafava and Weiler, 1980). An attempt to address some of these limitations is being made by constructing models of retinal ganglion cells that accurately reproduce the firing patterns of real ganglion cells (Baker and Ulinski, 2001). These model ganglion cells can then be used as inputs to the model geniculate neurons.

5.2. Cortical Waves

Despite these limitations, the current model was successful in capturing the basic features of cortical waves in turtle visual cortex. The latency of wave onset following stimulus presentation in the model was approximately 20 ms after injecting depolarizing currents in the model geniculate neurons. Senseman (1999) found that electrical activation of geniculate afferents in his in vitro preparation resulted in cortical waves with latencies of 14.1 ms to 20.7 ms. By contrast, the latency of responses in cortical neurons to light flashes is typically 100 ms to 200 ms with intracellular recording methods and in vitro preparations (Kriegstein, 1987; Mancilla et al., 1998; Mancilla and Ulinski, 2001; Senseman, 1996). This is consistent with latencies of 138 ms to 150 ms for the onset of cortical waves with visual stimuli in both in vitro (Senseman, 1999) and in vivo (Prechtl, 1994) preparations using both multielectrode arrays (Prechtl et al., 1997) and voltage sensitive dye methods (Senseman, 1999). The difference in latencies in the model and in turtles can be attributed to the time required for intraretinal processing and the conduction time from the retina to the cortex. The first spikes generated in retinal ganglion cells following light flashes typically have latencies on the order of 100 ms to 200 ms (Granda and Fulbrook, 1989; Marchiafava, 1983). The first spikes generated in turtle geniculate neurons following visual stimuli typically have latencies on the order of 150 ms (Boiko, 1980).

Cortical waves invariably originate in a specific region of the model cortex, regardless of the stimulus. This is the region in which there is a high density of varicosities on geniculocortical axons because the axons funnel down to a relatively small area as they enter the model cortex and cross over each other. The same situation occurs in turtles because the axons in the lateral forebrain bundle enter the cortex within a relatively small area, causing a visible bump, or ventricular eminence, on the ependymal surface of the lateral ventricle. Voltage-sensitive dye experiments show that cortical waves originate in this same region, regardless of the stimulus used to trigger the wave. Simulations with the model cortex suggest the common point of origination is due to the high density of geniculocortical synapses on pyramidal cells in the ventricular eminence, making it likely that many pyramidal cells will reach firing threshold as a volley of action potentials enters the cortex. Activation of different groups of geniculate neurons results in the firing of slightly different groups of pyramidal cells in the model, so there is some topography in the point at which pyramidal cells first fire. However, it is unlikely that this topography could be resolved in voltage sensitive dye experiments.

After originating near the rostral pole of the model cortex, the wave propagates radially throughout the cortex. The propagation velocity is on the order of 4 μm/ms to 70 μm/ms with some differences in the propagation velocity along different radii. Cortical waves visualized in voltage-sensitive dye experiments also propagate radially away from the ventricular eminence and show a distinct anisotropy in propagation velocity that varies from 14 μm/ms to 40 μm/ms (Senseman, 1999). Cortical waves have now been observed in the primary visual cortex (Grinvald et al., 1994; Bringuier et al., 1999; Ermentrout and Kleinfeld, 2001; Contreras and Llinas, 2001), somatosensory cortex (Contreras and Llinas, 2001; Ghanzafar and Nicoleilis, 1999), frontal cortex (Seidemann et al., 2002), and hippocampus (Traub et al., 1991) of mammals. Propagations velocities range from 100 μm/ms to 250 μm/ms. The differences in propagation velocities between turtles and mammals may be due to differences in body temperature (Senseman, 1999).

Cortical waves occasionally reflect at the caudal edge of the model cortex and propagate for some distance rostrally into the cortex before dying out. A first thought might be that the reflections are artifactual consequences of the model having edges. However, reflections are also seen at the edges of turtle area D (Senseman, 1999) and within slices of rat neocortex (Chagnac-Amitai and Connors, 1989; Chervin et al., 1988) and may actually be a feature of cortical organization. Cortical waves that originate in the visual cortex (cytoarchitectonic area D) of turtles continue across the border of D with the adjacent dorsomedial area (cytoarchitectonic area DM). They then propagate across DM with a propagation velocity of about 10 μm/ms. There is evidence for anatomical connections from D to DM (Desan, 1984), so a route by which pyramidal cells in D can excite cells in DM is present. It is not clear that there are anatomical connections between the caudal edge of D and the cortical regions located caudal to the visual cortex, so the failure of the cortical wave to propagate beyond the caudal edge of the cortex is not surprising. The mechanisms underlying reflections are not clear.

The spatiotemporal dynamics of the wave can be represented by a trajectory in a phase space by performing a Karhunen-Loéve decomposition on a movie of the wave (Nenadic et al., 2002). These trajectories have a characteristic elliptical or tear-drop shape and resemble homoclinic orbits. Homoclinic orbits in dynamical systems theory are characteristic of systems that are in a relatively stable state (e.g., Strogatz, 1994). Perturbation of the system causes it to move away from but then return asymptotically to the same stable state or fixed point. Karhunen-Loéve analysis of waves from turtle cortex following retinal flashes, the presentation of spots of light to the retina or the presentation of looming stimuli produces phase space trajectories that closely resemble those occurring in the model cortex (Robbins and Senseman, 1998; Senseman and Robbins, 1999, 2002).

The waves observed in the model following simulated diffuse light flashes are planar waves that propagate radially away from their point of origin. Evidence for planar waves in turtle cortex has been obtained using both voltage-sensitive dye and multielectrode recording methods, as reviewed, above. In addition, Prechtl et al. (1997, 2000) have used an in vivo preparation and reported observing very complex propagating waves. Their observations include circular or spiral (Ermentrout and Kleinfeld, 2001) waves that can originate near the border of visual cortex with cortical area DM under some circumstances. It is not yet known if the current version of the model lacks intrinsic features of its structure that are responsible for circular waves in real turtle cortex or if other sets of inputs would generate circulate waves.

5.3. Functional Significance of Cortical Waves

Nenadic et al. (2002) suggest that the spatiotemporal dynamics of the waves in turtle visual cortex contain information about the position and speed of stimuli in visual space. They used the model of turtle visual cortex reported here to show that the simulation of spots of light presented at different points along the horizontal meridian of visual space produce different phase-space trajectories following a Karhunen-Loéve decomposition. They then used a second Karhunen-Loéve decomposition to compare the shapes of these trajectories. The result of the two-step decomposition was a map of points along the horizontal meridian of visual space to a low-dimensional space they called B-space. Bayesian estimation methods showed that the position of a point in B-space could be used to estimate the location of a spot of light along the horizontal meridian in visual space. This analysis demonstrates that the cortical waves contain information about position along the horizontal meridian, but there is no evidence as of yet that this information is used by the turtle in visual tasks.

Appendix A

Table 1. Dimensions and maximal channel densities for individual compartments in the lateral pyramidal cell model. Dendritic compartments are cylindrical; the soma compartment is spherical. Diameters and lengths are in μm. Maximal channel conductances are in mS/cm^2. Links specify connections between compartments. For example, compartment 2 is linked to compartments 1 and 3.

Number	Name	Diameter	Length	Links	$\bar{g}_{Na^+}$	$\bar{g}_{K^+}$	$\bar{g}_{Ca^{2+}}$	$\bar{g}_{K^+(AHP)}$	g^{leak}
1	apical 6	0.9	50	2	0	0	0	0	0.03
2	apical 5	2.3	79	1, 3	0	0	0	0	0.03
3	apical 4	2.5	83	2, 4	0	0	0	0	0.03
4	apical 3	5.1	119	3, 5	0	0	0	0	0.03
5	apical 2	7.1	140	4, 6	0	0	0	0	0.03
6	apical 1	8.5	153	5, 7	0	0	0	0	0.03
7	soma	20.6	–	6, 8	370	250	2.3	0.02	0.03
8	basal 1	14.7	201	7, 9	0	0	0	0	0.03
9	basal 2	8.0	148	8, 10	0	0	0	0	0.03
10	basal 3	3.6	124	9, 11	0	0	0	0	0.03
11	basal 4	5.9	127	10, 12	0	0	0	0	0.03
12	basal 5	5.0	117	11, 13	0	0	0	0	0.03
13	basal 6	3.5	98	12, 14	0	0	0	0	0.03
14	basal 7	3.4	97	13, 15	0	0	0	0	0.03
15	basal 8	1.4	62	14, 16	0	0	0	0	0.03
16	basal 9	0.8	47	15	0	0	0	0	0.03

Table 2. Dimensions and maximal channel densities for individual compartments in the medial pyramidal cell model. Dendritic compartments are cylindrical; the soma compartment is spherical. Diameters and lengths are in μm. Maximal channel conductances are in mS/cm^2.

Number	Name	Diameter	Length	Links	$\bar{g}_{Na^+}$	$\bar{g}_{K^+}$	$\bar{g}_{Ca^{2+}}$	$\bar{g}_{K^+(AHP)}$	g^{leak}
1	dendrite 1	2.5	79	2	0	0	0	0	0.027
2	dendrite 2	2.4	76	1, 3	0	0	0	0	0.027
3	dendrite 3	2.4	76	2, 4	0	0	0	0	0.027
4	dendrite 4	2.3	74	3, 5	0	0	0	0	0.027
5	dendrite 5	5.5	115	4, 6	0	0	0	0	0.027
6	soma	30.6	–	5, 7	928	925	2.75	0.01	0.027
7	dendrite 6	14.3	186	6, 8	0	0	0	0	0.027
8	dendrite 7	14.0	186	7, 9	0	0	0	0	0.027
9	dendrite 8	13.0	177	8, 10	0	0	0	0	0.027
10	dendrite 9	10.3	158	9, 11	0	0	0	0	0.027
11	dendrite 10	6.4	125	10, 12	0	0	0	0	0.027
12	dendrite 11	3.0	85	11	0	0	0	0	0.027

Table 3. Dimensions and maximal channel densities for individual compartments in the stellate cell model. Dendritic compartments are cylindrical; the soma compartment is spherical. Diameters and lengths are in μm. Maximal channel conductances are in mS/cm^2.

Number	Name	Diameter	Length	Links	$\bar{g}_{Na^+}$	$\bar{g}_{K^+}$	g^{leak}
1	soma	12.7	–	2, 4, 7, 9, 12, 14	300	200	0.116
2	dendrite 1	3.0	90	1, 3	0	0	0.116
3	dendrite 2	2.0	90	2	0	0	0.116
4	dendrite 3	3.0	90	1, 5, 6	0	0	0.116
5	dendrite 4	2.0	90	4	0	0	0.116
6	dendrite 5	2.0	90	4	0	0	0.116
7	dendrite 6	3.0	90	1, 8	0	0	0.116
8	dendrite 7	2.0	90	7	0	0	0.116
9	dendrite 8	3.0	90	1, 10, 11	0	0	0.116
10	dendrite 9	2.0	90	9	0	0	0.116
11	dendrite 10	2.0	90	9	0	0	0.116
12	dendrite 11	3.0	90	1, 13	0	0	0.116
13	dendrite 12	2.0	90	12	0	0	0.116
14	dendrite 13	3.0	90	1, 15, 16	0	0	0.116
15	dendrite 14	2.0	90	14	0	0	0.116
16	dendrite 15	2.0	90	14	0	0	0.116

Table 4. Dimensions and maximal channel densities for individual compartments in the horizontal cell model. Dendritic compartments are cylindrical; the soma compartment is spherical. Diameters and lengths are in μm. Maximal channel conductances are in mS/cm^2.

Number	Name	Diameter	Length	Links	$\bar{g}_{Na^+}$	$\bar{g}_{K^+}$	g^{leak}
1	soma	25	–	2, 3	9500	300	0.029
2	dendrite 1	10.0	300	1	0	0	0.029
3	dendrite 2	10.0	300	1	0	0	0.029

Table 5. Biophysical parameters for model cells. The specific membrane resistance, R_m (kΩ cm^2); specific membrane capacitance, C_m(μF/cm^2); axial resistance, R_a(Ω cm); and resting membrane potential, E_{rest} (mV) are indicated for the lateral pyramidal cell, medial pyramidal cell, stellate cell and horizontal cell models.

Type of cell	Number of compartments	R_m	C_m	R_a	E_{rest}
Lateral pyramidal	16	108	1.4	100	−58.4
Medial pyramidal	12	132	1.3	100	−56.0
Stellate	16	100	1.5	100	−57.0
Horizontal	3	43.2	1.6	100	−75.0

Appendix B

This appendix specifies the form of the current terms in Eq. (1). Maximal densities of voltage-gated conductances on each compartment of each type of neuron are given in Table 1. Voltage dependencies of the variables m, h, n, s, and r and calcium dependencies of the variable q are given in Table 6.

Fast sodium current, $I_{Na^+}(V, t)$:

$$\begin{aligned} I_{Na^+}(V,t) &= \bar{g}_{Na^+} m^3 h (V - 40) \\ \frac{dm}{dt} &= \alpha_m (1 - m) - \beta_m m \\ \frac{dh}{dt} &= \alpha_h (1 - h) - \beta_h h. \end{aligned} \tag{6}$$

Delayed rectifier potassium current, $I_{K^+}(V, t)$:

$$\begin{aligned} I_{K^+}(V,t) &= \bar{g}_{K^+} n^4 (V + 90) \\ \frac{dn}{dt} &= \alpha_n (1 - n) - \beta_n n. \end{aligned} \tag{7}$$

High-voltage calcium current, $I_{Ca^{2+}}(V, t)$:

$$\begin{aligned} I_{Ca^{2+}}(V,t) &= \bar{g}_{Ca^{2+}} s^2 r (V - 40) \\ \frac{ds}{dt} &= \alpha_s (1 - s) - \beta_s s \\ \frac{dr}{dt} &= \alpha_r (1 - r) - \beta_r r. \end{aligned} \tag{8}$$

Table 6. Activity variable rate functions. Voltage dependence of the forward (α) and backward (β) rate constants for each activity variable are given. V is in mV. The AHP conductance is a nonvoltage, calcium dependent conductance that depends on intracellular calcium concentration, $[Ca^{2+}]$ in mM. Differential equations for the activity variables are given in the Appendix.

Channel/Variable	Forward (α)	Backward (β)
Na^+/m	$\frac{-11.0944-0.32\ V}{-1+e^{(34.67+V)/(-4.00)}}$	$\frac{1.8676+0.28\ V}{-1+e^{(6.67+V)/5.00}}$
Na^+/h	$\frac{0.128}{e^{(34.00+V)/18.00}}$	$\frac{4.00}{1+e^{(11.00+V)/(-5.00)}}$
K^+/n	$\frac{-1.152-0.032\ V}{-1+e^{(36.00+V)/(-3.50)}}$	$\frac{0.50}{e^{(41.00+V)/40.00}}$
Ca^{2+}/s	$\frac{-1.50-0.075\ V}{-1+e^{(20.00+V)/(-7.50)}}$	$\frac{0.2121+0.0101\ V}{-1+e^{(21.00+V)/4.40}}$
Ca^{2+}/r	$\frac{0.018576+0.000344\ V}{-1+e^{(54.00+V)/4.45}}$	$\frac{-0.018558-0.0003093\ V}{-1+e^{(60.00+V)/(-4.00)}}$
K^+(AHP)/q	$\begin{cases}10\times10^{-3} & \text{if } [Ca^{2+}]>500\\ 0.02\times[Ca^{2+}]\times10^{-3} & \text{otherwise}\end{cases}$	1.0×10^{-3}

Table 7. Radii of influence for different types of synaptic connections. The units are given in μm.

From\To	Lateral	Medial	Stellate	Horizontal
LGN (varicosities)	26	60	25	–
Lateral	250	250	250	250
Medial	250	250	250	250
Stellate	350	350	350	–
Horizontal	350	350	–	–

Table 8. Synaptic weights, ω_{base}, for synaptic connections. Values of ω_{base} are given for each type of synapse in the model. Synapses from lateral and medial pyramidal cells to other types of neurons are graded functions of distance with standard deviations of σ in mm. The synaptic weights from stellate and horizontal cells to other types of neurons do not vary with distance.

From\To	Lateral	Medial	Stellate	Horizontal
LGN (varicosities)	1.87	0.25	0.25	–
Lateral ($\sigma = 1.5$)	AMPA: 1.425	AMPA: 1.80	AMPA: 0.015	AMPA: 0.030
	NMDA: 0.045	NMDA: 0.09	NMDA: 0.150	NMDA: 0.285
Medial ($\sigma = 1.5$)	AMPA: 0.450	AMPA: 0.600	AMPA: 0.015	AMPA: 0.030
	NMDA: 0.025	NMDA: 0.025	NMDA: 0.165	NMDA: 0.330
Stellate	$GABA_A$: 1.900	$GABA_A$: 1.370	$GABA_A$: 0.100	
	$GABA_B$: 0.002	$GABA_B$: 0.001	$GABA_B$: 2.5e-4	–
Horizontal	$GABA_A$: 7.600	$GABA_A$: 5.500		
	$GABA_B$: 0.002	$GABA_B$: 0.002	–	–

Intracellular calcium concentration:

$$\frac{d[Ca^{2+}]_i}{dt} = BI_{Ca^{2+}}(V,t) - \frac{[Ca^{2+}]_i}{\tau_{Ca_i^{2+}}}$$
$$B = 6000.55\ \text{mM/nA ms} \qquad (9)$$
$$\tau_{Ca_i^{2+}} = 1000\ \text{ms}.$$

The subscript i in the above equation indicates that the concentration is the internal calcium concentration.

Calcium dependent after hyperpolarization potassium current, $I_{AHP}([Ca^{2+}]_i, t)$:

$$I_{AHP}([Ca^{2+}]_i, t) = \bar{g}_{AHP}\, q(V+90). \qquad (10)$$

Leak current, I_{leak}:

$$I_{\text{leak}} = \bar{g}_{\text{leak}}(V - E_{\text{rest}}), \tag{11}$$

where E_{rest} is given in Table 5.

The synaptic currents ($I_{\text{AMPA}}(V, t)$, $I_{\text{GABA}_\text{A}}(V, t)$, and $I_{\text{GABA}_\text{B}}(V, t)$) are specified by current terms of the form

$$I_{\text{syn}}(t) = g_{\text{syn}}(t)(V - E_{\text{syn}}), \tag{12}$$

where $g_{\text{syn}}(t)$ is given by Eq. (2). Parameter values for AMPA-receptor mediated, GABA_A-receptor mediated and GABA_B-receptor mediated currents are specified in the text.

NMDA-receptor mediated current, $I_{\text{NMDA}}(V, t)$:

$$I_{\text{NMDA}}(V, t) = g_{\text{NMDA}}(t)v(V - E_{\text{NMDA}}) \tag{13}$$

where $g_{\text{NMDA}}(t)$ has the same form as described in Eq. (2) and the parameter values are likewise given in the text. The voltage dependance factor of the current, v, is given by Eq. (4).

Acknowledgments

We would like to thank Dr. David Senseman from the University of Texas at San Antonio for providing us with Fig. 18A. We would also like to thank the Learning and Intelligent System (LIS) initiative of the National Science Foundation for providing us with partial support. This research is partially supported by the NSF under grants ECS9720357 and ECS9976174.

When $\tau_{\text{o}} = \tau_{\text{c}}$, the synaptic conductance is given by a modified formula (see page 168). We would like to thank Reviewer 1 for pointing this out. As suggested by Reviewer 2, we have made a note on the properties of the waves observed by Prechtl et al. (1997, 2000) on page 179.

References

Ammermuller J, Muller JF, Kolb H (1995) The organization of the turtle inner retina. II. Analysis of color-coded and directionally selective cells. J. Comp. Neurol. 358: 35–62.

Baker TI, Ulinski PS (2001) Models of direction selective and non-direction selective turtle retinal ganglion cells. Soc. Neurosci. Abstr.

Blanton MG, Kriegstein AR (1992) Properties of amino acid neurotransmitter receptors of embryonic cortical neurons when activated by exogenous and endogenous agonists. J. Neurophysiol. 67: 1185–1200.

Blanton MG, Shen JM, Kriegstein AR (1987) Evidence for the inhibitory neurotransmitter gamma-aminobutyric acid in a spiny and sparsely spiny nonpyramidal neurons of turtle dorsal cortex. J. Comp. Neurol. 259: 277–297.

Block J, Colombe JB, Ulinski PS (2002) Physiology of identified stellate cells from turtle visual cortex. Soc. Neurosci. Abstr.

Boiko VP (1980) Responses to visual stimuli in thalamic neurons of the turtle *Emys orbicularis*. Neurosci. Behav. Physiol. 10: 183–188.

Bower JM, Beeman D (1997) The Book of Genesis, 2nd ed. TELOS, New York.

Bringuier V, Chavane F, Glaeser L, Fregnac Y (1999) Horizontal propagation of visual activity in the synaptic integration field of area 17 neurons. Science 283: 695–699.

Chagnac-Amitai Y, Connors BW (1989) Horizontal spread of synchronized activity in neocortex and its control by GABA-mediated inhibition. J. Neurophysiol. 61: 747–758.

Chervin RD, Pierce PA, Connors BW (1988) Periodicity and directionality in the propagation of epileptiform dischargers across neocortex. J. Neurophysiol. 60: 1695–1713.

Colombe JB, Ulinski PS (1999) Temporal dispersion windows in cortical neurons. J. Comp. Neurosci. 7: 71–87.

Connors BW, Kriegstein AR (1986) Cellular physiology of the turtle visual cortex: Distinctive properties of pyramidal and stellate neurons. J. Neurosci. 6: 164–177.

Contreras D, Llinas R (2001) Voltage-sensitive dye imaging of neocortical spatiotemporal dynamics to afferent activation frequency. J. Neurosci. 21: 9403–9413.

Cosans CE, Ulinski PS (1990) Spatial organization of axons in turtle visual cortex: Intralamellar and interlamellar projections. J. Comp. Neurol. 296: 548–558.

Desan PH (1984) The organization of the cerebral cortex of the pond turtle. *Pseudemys scripta elegans*. Ph.D. dissertation, Harvard University, Cambridge, MA.

Ermentrout GB, Kleinfeld D (2001) Travelling electrical waves in cortex: Insights from phase dynamics and speculation on a computational role. Neuron 29: 33–44.

Feldman ML, Peters A (1979) A technique for estimating total spine numbers on Golgi-impregnated dendrites. J. Comp. Neurol. 188: 527–542.

Fowler M (1994) Analysis of spontaneous inhibitory postsynaptic potentials from pyramidal cells of turtle visual cortex. Ph.D. dissertation, University of Chicago.

Ghanzafar AA, Nicoleilis MAL (1999) Spatiotemporal properties of layer V neurons of the rat primary somatosensory cortex. Cerebral Cortex 9: 348–361.

Granda AM, Fulbrook JE (1989) Classification of turtle retinal ganglion cells. J. Neurophysiol. 62: 723–737.

Grinvald A, Lieke EE, Frostig RD, Hidesheim R (1994) Cortical point spread function and long-range lateral interactions revealed by real-time optical imaging of macaque monkey primary visual cortex. J. Neurosci. 14: 2545–2568.

Heller SB, Ulinski PS (1987) Morphology of geniculocortical axons in turtles of the genera *Pseudemys* and *Chrysemys*. Anat. Embryol. 175: 505–515.

Jahr CE, Stevens CF (1990) A qualitative description of NMDA receptor channel kinetic behavior. J. Neurosci. 10: 1830–1837.

Jensen RJ, DeVoe RD (1983) Comparisons of directionally selective with other ganglion cells of the turtle retina: Intracellular recording and staining. J. Comp. Neurol. 217: 271–287.

Khatri V, Ulinski PS (2000) Functional significance of inhibitory interactions between inhibitory interneurons in visual cortex. Neurocomputing 32–33: 425–432.

Kriegstein AR (1987) Synaptic responses of cortical pyramidal neurons to light stimulation in the isolated turtle visual system. J. Neurosci. 6: 178–191.

Larson-Prior LJ, Ulinski PS, Slater NT (1991) Excitatory amino acid receptor-mediated transmission in geniculocortical and intracortical pathways within visual cortex. J. Neurophysiol. 66: 293–306.

Madison DV, Nicoll RA (1984) Control of the repetitive discharge of rat CA1 pyramidal neurons in vitro. J. Physiol. (Lond.) 354: 319–331.

Mancilla JG, Fowler MH, Ulinski PS (1998) Responses of regular spiking and fast spiking cells in turtle visual cortex to light flashes. Vis. Neurosci. 15: 979–993.

Mancilla JG, Ulinski PS (1996) Temporal structure of compound postsynaptic potentials in visual cortex. In Bower JM, ed. Proceedings of the Fourth Computation and Neural Systems Conference. Academic Press, New York. pp. 227–232.

Mancilla JG, Ulinski PS (2001) Role of $GABA_A$-mediated inhibition in controlling the responses of regular spiking cells in turtle visual cortex. Vis. Neurosci. 18: 9–24.

Marchiafava PL (1983) The organization of inputs establishes two functional and morphologically identifiable classes of ganglion cells in the retina of the turtle. Vis. Res. 23: 325–338.

Marchiafava PL, Weiler R (1980) Intracellular analysis and structural correlates of the organization of inputs to ganglion cells in the retina of the turtle. Proc. R. Soc. Lond. B 208: 103–113.

Mazurskaya PS (1974) Organization of receptive fields in the forebrain of *Emys orbicularis*. Neurosci. Behav. Physiol. 7: 311–318.

Millonas MM, Ulinski PS (1997) The dendritic origins of fast prepotentials in pyramidal cells. In: Proceedings of Computational Neuroscience. Academic Press, San Diego.

Mulligan KA, Ulinski PS (1990) Organization of geniculocortical projections in turtles: Isoazimuth lamellae in the visual cortex. J. Comp. Neurol. 296: 531–547.

Nenadic Z, Ghosh BK, Ulinski PS (2000) Spatiotemporal dynamics in a model of turtle visual cortex. Neurocomputing 32–33: 479–486.

Nenadic Z, Ghosh BK, Ulinski PS (2002) Modelling and estimation problems in the turtle visual cortex. IEEE Trans. Biomed. Eng. 49: 753–762.

Nicolaus JM, Ulinski PS (1991) Medial and lateral differences in populations of GABAergic neurons in layer 3 of turtle visual cortex. Soc. Neurosci. Abstr. 16: 114.

Nicolaus JM, Ulinski PS (1994) Inward rectifying conductances in inhibitory neurons in turtle visual cortex. In: Eeckman F, ed. Neural Systems: Analysis and Modelling 3. Kluwer, Boston. pp. 91–96.

Prechtl JC (1994) Visual motion induces synchronous oscillations in turtle visual cortex. Proc. Natl. Acad. Sci. USA 91: 12467–12471.

Prechtl JC, Bullock TH, Kleinfeld D (2000) Direct evidence for local oscillatory current sources and intracortical phase gradients in turtle visual cortex. Proc. Natl. Acad. Sci. 97: 877–882.

Prechtl JC, Cohen LB, Mitra PP, Pesaran B, Kleinfeld D (1997) Visual stimuli induce waves of electrical activity in turtle cortex. Proc. Natl. Acad. Sci. 94: 7621–7626.

Rainey WT, Ulinski PS (1986) Morphology of neurons in the dorsal lateral geniculate nucleus in turtles of the genera *Pseudemys* and *Chrysemys*. J. Comp. Neurol. 253: 440–465.

Robbins KA, Senseman DM (1998) Visualizing differences in movies of cortical activity. IEEE Visualization '98, 217–224.

Seidemann E, Arieli A, Grinvld A, Slovin H (2002) Dynamics of depolarization and hyperpolarization in the frontal cortex and saccade goal. Science 285: 862–865.

Senseman DM (1996) Correspondence between visually evoked voltage-sensitive dye signals and synaptic activity recorded in cortical pyramidal cells with intracellular microelectrodes. Vis. Neurosci. 13: 963–977.

Senseman DM (1999) Spatiotemporal structure of depolarization spread in cortical pyramidal cell populations evoked by diffuse retinal light flashes. Vis. Neurosci. 16: 65–79.

Senseman DM, Robbins KA (1999) Modal behavior of cortical neural networks during visual processing. J. Neurosci. 19: RC3(1–7).

Senseman DM, Robbins KA (2002) High-speed VSD imaging of visually evoked cortical waves: Decomposition into intra- and intercortical wave motions. J. Neurophysiol. 87: 1499–1514.

Smith LM, Ebner FF, Colonnier M (1980) The thalamocortical projection in Pseudemys turtles: A quantitative electron microscopic study. J. Comp. Neurol. 190: 445–461.

Stratford KJ, Mason AJR, Larkman AU, Major G, Jack JJB (1989) The modelling of pyramidal neurons in the visual cortex. In: Durbin R, Miall C, Mitchison G, eds. The Computing Neurone. Addison Wesley, Reading, MA. pp. 296–321.

Strogatz SH (1994) Nonlinear Dynamics and Chaos. Addison-Wesley, Reading, MA.

Traub RD, Wong RKS, Miles R, Michelson H (1991) A model of a CA3 hippocampal pyramidal neuron incorporating voltage-clamp data on intrinsic conductances. J. Neurophysiol. 66: 635–650.

Ulinski PS (1986) Organization of the corticogeniculate projections in the turtle, *Pseudemys scripta*. J. Comp. Neurol. 254: 529–542.

Ulinski PS (1990) The cerebral cortex in reptiles. In: Jones EG, Peters A, eds. Cerebral Cortex. Vol. 8A, Comparative Structure and Evolution of Cerebral Cortex, Part I. Plenum Press, New York. pp. 139–215.

Ulinski PS, Larson-Prior LU, Slater NT (1991) Cortical circuitry underlying visual motion analysis in turtles. In: Arbib M, ed. Visual Structures and Integrated Functions. Springer, Berlin. pp. 307–324.

Ulinski PS (1999) Neural mechanisms underlying the analysis of moving visual stimuli. In: Ulinski PS, Jones EG, Peters A, eds. Cerebral Cortex. Vol. 13. Models of Cortical Circuitry. Plenum Press, New York. pp. 283–399.

Ulinski PS, Nautiyal J (1986) Organization of the retinogeniculate projections in turtles of the genera *Pseudemys* and *Chrysemys*. J. Comp. Neurol. 276: 92–112.